

A COMPREHENSIVE X-RAY SPECTRAL ANALYSIS OF THE SEYFERT 1.5 NGC 3227

A. MARKOWITZ¹, J.N. REEVES², I.M. GEORGE^{3,4}, V. BRAITO⁵, R. SMITH⁵, S. VAUGHAN⁵, P. ARÉVALO⁶, F. TOMBESI^{4,7,8,9}¹ CENTER FOR ASTROPHYSICS AND SPACE SCIENCES, UNIVERSITY OF CALIFORNIA, SAN DIEGO, M.C. 0424, LA JOLLA, CA, 92093-0424, USA² ASTROPHYSICS GROUP, SCHOOL OF PHYSICAL AND GEOGRAPHICAL SCIENCES, KEELE UNIVERSITY, KEELE, STAFFORDSHIRE, ST5 5BG, UK³ DEPARTMENT OF PHYSICS, UNIVERSITY OF MARYLAND, BALTIMORE COUNTY, 1000 HILLTOP CIRCLE, BALTIMORE, MD, 21250, USA⁴ X-RAY ASTROPHYSICS LABORATORY, CODE 662, NASA GODDARD SPACE FLIGHT CENTER, GREENBELT, MD, 20771, USA⁵ X-RAY ASTRONOMY GROUP, UNIVERSITY OF LEICESTER, LEICESTER LE1 7RH, UK⁶ DEPARTMENT OF PHYSICS AND ASTRONOMY, UNIVERSITY OF SOUTHAMPTON, HIGHFIELD, SOUTHAMPTON, SO17 1BJ⁷ DEPARTMENT OF PHYSICS AND ASTRONOMY, JOHNS HOPKINS UNIVERSITY, 3400 N. CHARLES STREET, BALTIMORE, MD 21218, USA⁸ INAF-IASF BOLOGNA, VIA GOBETTI 101, 40129, BOLOGNA, ITALY⁹ DIPARTIMENTO DI ASTRONOMIA, UNIVERSITÀ DEGLI STUDI DI BOLOGNA, VIA RANZINI 1, 40127, BOLOGNA, ITALY

ABSTRACT

We present results of a 100 ks *XMM-Newton* observation of the Seyfert 1.5 AGN NGC 3227. Our best-fit broadband model to the EPIC pn spectrum consists of a moderately flat (photon index of 1.57) hard X-ray power-law absorbed by cold gas with a column density of $3 \times 10^{21} \text{ cm}^{-2}$, plus a strong soft excess, modeled as a steep power law with a photon index of 3.35, absorbed by cold gas with a column density of $9 \times 10^{20} \text{ cm}^{-2}$. The soft excess increases in normalization by $\sim 20\%$ in ~ 20 ks, independently of the hard X-ray emission component, and the UV continuum, tracked via the OM, also shows a strong increasing trend over the observation, consistent with reprocessing of soft X-ray emission. Warm absorber signatures are evident in both the EPIC and RGS spectra; we model two absorbing layers, with ionization parameters $\log \xi = 1.2$ and $2.9 \text{ erg cm s}^{-1}$, and with similar column densities ($\sim 1\text{--}2 \times 10^{21} \text{ cm}^{-2}$). The outflow velocities relative to systemic of the high- and low-ionization absorbers are estimated to be $-(2060^{+240}_{-170}) \text{ km s}^{-1}$ and $-(420^{+430}_{-190}) \text{ km s}^{-1}$, respectively. The Fe K α line FWHM width is $7000 \pm 1500 \text{ km s}^{-1}$; its inferred distance from the black hole is consistent with the BLR and with the inner radius of the dust reverberation-mapped by Suganuma et al. An emission feature near 6.0 keV is modeled equally well as a narrow redshifted Fe K line, possibly associated with a disk “hot-spot,” or as the red wing to a relativistically broadened Fe line profile. *Swift*-BAT and archival *RXTE* data suggest at most a weak Compton reflection hump ($R \lesssim 0.5$), and a high-energy cutoff near 100 keV. From *RXTE* monitoring, we find tentative evidence for a significant fraction of the Fe line flux to track variations in the continuum on time scales < 700 days.

Subject headings: galaxies: active — galaxies: Seyfert — X-rays: galaxies — galaxies: individual (NGC 3227)

1. INTRODUCTION

A 1993 *Advanced Satellite for Cosmology and Astrophysics* (*ASCA*) observation of the nucleus of the Seyfert 1.5 NGC 3227 first revealed evidence for ionized absorbing gas with $N_{\text{H,WA}} \sim 1\text{--}4 \times 10^{21} \text{ cm}^{-2}$ (Netzer et al. 1994, Ptak et al. 1994). Komossa & Fink (1997b), using 1993 *Röntgen Satellite* (*ROSAT*)-PSPC data, and George et al. (1998b), using *ASCA* data taken in 1993 and 1995, further modeled the warm absorber, finding it to be relatively lowly-ionized relative to most other Seyferts’ warm absorbers. Given the low-resolution spectra, the solution for further progress was to obtain a gratings spectrum. Komossa (2002) reported on a *Chandra*-LETGS observa-

tion of NGC 3227 in October 2000, noting edge-like features near 0.7 keV. *XMM-Newton* first observed NGC 3227 in November 2000, when the source was undergoing a 3-month long period of very high levels of obscuration due to a compact cloud with N_{H} near $3 \times 10^{23} \text{ cm}^{-2}$, covering 90% of the central source, and likely associated with the BLR, traversing the line of sight (Lamer et al. 2003). The soft X-ray data from this observation indicated the warm absorber to have ionization parameter $\log \xi^{10} = 1.7\text{--}2.0 \text{ erg cm s}^{-1}$ and a column density $N_{\text{H,WA}} = 2\text{--}9 \times 10^{21} \text{ cm}^{-2}$ (Gondoin et al. 2003).

Optical spectra of the nucleus of NGC 3227 have indicated strong reddening due to the presence of dust along

¹⁰ The ionization parameter $\xi \equiv L_{\text{ion}} n_e^{-1} r^{-2}$, where L_{ion} is the isotropic 1–1000 Ryd ionizing continuum luminosity, n_e is the electron number density, and r is the distance from the central continuum source to the absorbing gas.

the line of sight. The narrow line $H\alpha/H\beta$ ratio, for instance, indicates reddening, with measured ratios in NGC 3227 implying visual extinctions $A_V = (H\alpha/H\beta)/3.1$ near 1.2–1.7 (Cohen 1983; Gonzalez Delgado & Perez 1997), though A_V values of 4.5–4.9 have been reported (Mundell et al. 1995a, Rubin & Ford 1968)¹¹. The broad $H\alpha/H\beta$ line ratio shows a similar level of reddening, $A_V = 1.4$ (Cohen 1983, Winge et al. 1995). The steep drop in NGC 3227’s continuum flux from the near-UV to the far-UV also supports reddening: the spectral index from *International Ultraviolet Explorer* (IUE) measurements is $\alpha_{IUE} = -2.9$ for NGC 3227, whereas $\alpha_{IUE} = -1.4$ is more typical for Seyfert 1s (Komossa & Fink 1997b; Courvoisier & Paltani 1992; Kinney et al. 1991). Assuming a standard Galactic gas/dust ratio of $N_H/A_V = 2 \times 10^{21} \text{ cm}^{-2} \text{ mag}^{-1}$ (e.g., Shull & van Steenburg 1985), the amount of NLR and BLR reddening implies that the dust is associated with a column of gas with $N_H \sim 2\text{--}3 \times 10^{21} \text{ cm}^{-2}$.

Komossa & Fink (1997b) and George et al. (1998b) also reported local absorption due to cold material with a column density $N_H = 3\text{--}6 \times 10^{20} \text{ cm}^{-2}$, in addition to the Galactic column ($2.1 \times 10^{20} \text{ cm}^{-2}$, Dickey & Lockman 1990, Murphy et al. 1996). The inferred local cold column density agrees with that derived from 21cm VLA observations (Mundell et al. 1995b); however, it is not sufficient to produce the observed optical reddening, assuming a standard Galactic gas/dust ratio. The agreement between the inferred column density associated with the dust and the column density of the ionized gas, however, prompted Komossa & Fink (1997b) to suggest that the dust was embedded in the warm absorber and not associated with the cold gas. Brandt, Fabian, & Pounds (1996) first suggested this “dusty warm absorber” concept for the quasar IRAS 13349+2438.

However, Kraemer et al. (2000) suggested that it was unlikely dust could survive within the high-ionization gas. They proposed a configuration consisting of *two* warm absorber zones, in addition to the cold column. One warm absorber is dust-free and highly-ionized, responsible for the oxygen edges; the other is a very lowly-ionized absorber with dust mixed in, referred to as a “dusty lukewarm absorber.” Those authors modeled the latter absorber with a density of 20 cm^{-3} and a location encompassing or lying just outside the NLR, which has a radius of $\sim 100 \text{ pc}$ (based on [O III] imaging; Schmitt & Kinney 1996). Using *Hubble Space Telescope* (HST)-STIS, Crenshaw et al. (2001) first observed the features of the dusty lukewarm absorber, evident in the form of optical/UV absorption lines due to intermediate species of C, N and Si; Crenshaw & Kraemer (2001) suggested that the absorber may possibly be a relatively highly-ionized component of the NLR seen in absorption. Kraemer et al. (2000) suggested that the dust may evaporate off the putative molecular torus and be swept up in an outflowing wind (e.g., Reynolds 1997). Based on V-band-to-K-band reverberation mapping (the latter band dominated by thermal dust emission) conducted by the MAGNUM collaboration, Suganuma et al. (2006) concluded that the innermost extent the dust was at a radius of $\sim 5\text{--}20$ light-days, suggesting an alternate or additional site from which an outflowing

wind could sweep up dust.

In 2006, we obtained a new, 100 ks *XMM-Newton* observation of NGC 3227 in an unobscured state, to better characterize the broadband X-ray continuum and X-ray warm absorber features, search for signatures of dust in the X-ray spectrum, relate the X-ray and dusty optical/UV warm absorbers, and study Fe K bandpass emission features. §2 describes the observations and data reduction. §3 and §4 describe EPIC spectral fits to the time-averaged spectrum, focusing on the Fe K bandpass and then extending to the 0.2–10 keV bandpass, respectively. §5 describes the fits to the RGS spectra. §6 describes spectral analysis of archival *RXTE* data to constrain the hard X-ray continuum. §7 describes time- and flux-resolved spectral fits to the EPIC data, including F_{var} spectra, and time-resolved spectral fits to the *RXTE* data to quantify the temporal behavior of the Fe line. X-ray/UV correlations are presented in §8. The results are discussed in §9, and a brief summary is given in §10.

2. OBSERVATIONS AND DATA REDUCTION

2.1. *XMM-Newton* data reduction

NGC 3227 was observed by *XMM-Newton* during Revolution 1279, on December 3–4, 2006, for a duration of 99 ks. *XMM-Newton*’s European Photon Imaging Camera (EPIC) consists of one pn CCD back-illuminated array sensitive to 0.15–15 keV photons (Strüder et al. 2001), and two MOS CCD front-illuminated arrays sensitive to 0.15–12 keV photons (MOS 1 and MOS 2, Turner et al. 2001). Data from the pn were taken in Large Window mode; data from both MOSes were taken in PrimePartialW2/small window mode. The medium filter was used for all three EPIC instruments. Spectra were extracted using *XMM-Newton*-SAS version 7.1.0 and using standard extraction procedures. For all three cameras, source data were extracted from a circular region of radius $40''$; backgrounds were extracted from circles of identical size, centered $\sim 3'$ away from the core. Hot, flickering, or bad pixels were excluded. Data were selected using event patterns 0–4 for the pn and 0–12 for the MOSes. Using the SAS task EPATPLOT, we verified that pile-up was negligible for the pn. For the MOS, pile-up was minimal ($<3\%$) up to 8 keV, and a bit higher (3–10%) above 8 keV. The effect of such pile-up is to artificially flatten the spectrum. However, we also extracted counts from the MOS CCDs using an annular region with inner radius $5''$ and outer radius $40''$ to minimize pile-up; the resulting spectra were virtually identical to those extracted using the circular region. We elected to fit the spectra extracted using circular regions in order to maximize the photon statistics associated with emission features in the Fe K bandpass.

We inspected the 10–12 keV pn background light curve; there were no significant flares (the 10–12 keV rate never exceeded 0.04 ct s^{-1}). The total good exposure time was 90.7 ks for pn and 96.4 ks for each MOS. The 0.2–10 keV pn light curve, binned to 600 s and normalized by its mean count rate (11.74 ct s^{-1}), is displayed in the top panel of Figure 1. Similarly displayed in Figure 1 are the 0.2–1 and 3–10 keV light curves; in these energy ranges, the total continuum is dominated by the soft excess and

¹¹ The $H\alpha/H\beta$ ratio is intrinsically 3.1, assuming case B recombination and assuming that collisional excitation is negligible, applicable for typical NLR conditions, but see warnings by Netzer 1990 regarding uncertainties in the intrinsic Balmer decrement.

hard X-ray power-law components, respectively, as will be demonstrated in §4.

The Reflection Grating Spectrometer (RGS) data were extracted using standard extraction procedures, including the SAS task RGSPROC and the most recent calibration files. We used the first-order data only; spectra were binned every 10 channels ($\sim 0.1\text{\AA}$, or roughly the RGS resolution). Virtually all bins contained at least 20 counts, allowing use of the χ^2 statistic. Bad RGS channels were ignored. The good exposure time was 99.2 ks for each RGS.

The Optical Monitor (OM) was in Science User Defined mode, with one “image” window $5.17' \times 5.17'$ centered on NGC 3227. The UVW1 filter, whose effective area peaks near 260 nm, was used throughout. Extraction proceeded in a manner similar to §2–3 of Smith & Vaughan (2007). Source photons were collected using a 12-pixel radius circle centered on NGC 3227. Emission from the host galaxy was not subtracted; the effect of including such a constant component is that any variability we observe is thus likely a lower limit to the intrinsic level of variability associated with the AGN. The background was extracted from a circular region away from the host galaxy. The resulting net light curve, extracted in 1400 s bins, is displayed in Figure 1.

2.2. *RXTE* PCA and *HEXTE* extraction

To investigate the form of the >10 keV continuum and estimate the strength of any Compton reflection hump present, we examined archival Rossi X-ray Timing Explorer *RXTE* Proportional Counter Array (PCA; Swank et al. 1998) and High-Energy X-Ray Timing Experiment (*HEXTE*; Rothschild et al. 1998) monitoring data. NGC 3227 was observed in November 1996 for ~ 260 ks. NGC 3227 was also monitored from 1999 January 2 until 2005 December 4, with one visit every 2–7 days, along with a period of more intensive monitoring approximately four times daily from 2000 April 2 to 2000 June 7 (see Uttley & McHardy 2005 for further details regarding sampling patterns). Each monitoring snapshot typically lasted 1 ks. There were no observations simultaneous with the 2006 *XMM-Newton* observation, so we considered all available data in the public archive in order to estimate average long-term properties. However, data taken from late 2000 to early 2001 (modified Julian day [MJD] 51850–52050), affected by the passage of the compact cloud across the line of sight, were ignored during spectral fitting.

PCA data were extracted and screened using standard methods and tools. The ‘L7-240’ background models, appropriate for faint sources, were used. See e.g., Markowitz, Edelson & Vaughan (2003) for details on PCA data extraction and background subtraction, the dominant source of systematic uncertainty (e.g., in total broadband count rate) in these data. Counts were extracted from Proportional Counter Units (PCUs) 0–2, 0 and 2, and 2 only for data observed before 1999 December 23, between 1999 December 23 and 2000 May 12, and after 2000 May 12, respectively. Response files were generated for gain epochs 3, 4 and 5 separately (data observed before 1999 March 22, between 1999 March 22 and 2000 May 12, and after 2000 May 12, respectively). As the response of the PCA slowly hardens over time due to the gradual leak of propane into

the xenon layers, data within each gain epoch were further split into roughly equal segments, each spanning durations of roughly a couple hundreds days, and separate response files were generated for each segment. Spectra and responses were then added, weighting by exposure times, using the FTOOLS SUMPHA and ADDRMF, respectively. The total exposure time for all PCA data was 842.7 ks.

The *HEXTE* instrument consists of two independent clusters (A and B), each containing four scintillation counters which share a common 1° FWHM field of view. Source and background spectra were extracted from each individual *RXTE* visit using Science Event data and standard extraction procedures. The same good time intervals used for the PCA data (e.g., including Earth elevation and SAA passage screening) were applied to the *HEXTE* data. To measure real-time background measurements, the two *HEXTE* clusters each undergo two-sided rocking to offset positions, in this case, to 1.5° off-source, switching every 32 seconds (16 seconds before 1998 Jan.). No strong contaminating hard X-ray source within 2° is evident (e.g., from the *RXTE*-PCA or *Swift*-BAT all-sky slew survey data available at the HEASARC’s online SkyView service). Cluster A data taken between 2004 Dec 13 and 2005 Jan 14 were excluded, as the cluster did not rock on/off source. Detector 2 aboard Cluster B lost spectral capabilities in 1996; these data were excluded from spectral analysis. Cluster A and B data were extracted separately and not combined, as their response matrices differ slightly. Deadtime corrections were applied. All data within each cluster were combined, except for the 1996 data; that is, the 1996 (16 s rocking) and 1999–2005 (32 s rocking) spectra were fit separately. We note that the 1996 and 1999–2005 spectra agree well with each other for each cluster, illustrating *HEXTE*’s performance down to source fluxes which are 1% of the background. Good exposure times for the four *HEXTE* source spectra were 237.1 ks (cluster A) and 234.2 ks (cluster B) for the 1999–2005 data, and 41.5 (A) and 41.8 ks (B) for the 1996 data. All data were grouped as follows: channels 17–30, 31–39, 40–47, 48–67, 68–79 and ≥ 80 were grouped by factors of 2, 3, 4, 5, 6 and 10, respectively. The LLAGN/LINER source NGC 3226 is located about $2'$ away and is thus in the field of view of both the PCA and *HEXTE*, but its flux is a factor of ~ 50 fainter than that of NGC 3227 in the 2–10 keV band (Binder et al, in prep.; George et al. 2001).

3. EPIC PN SPECTRAL FITS TO THE FE K BANDPASS

XSPEC (Arnaud 1996) v.11.3.2ag was used for all spectral fitting. All errors below correspond to $\Delta\chi^2 = 2.71$ (90% confidence level for one interesting parameter when the errors are symmetric) unless otherwise noted. The abundances of Lodders (2003) were used. NGC 3227’s redshift is 0.00386 (de Vaucouleurs et al. 1991); a distance of 20.3 Mpc was used (Mould et al. 2000) was used to calculate luminosities. In all models, we included a column of neutral absorption fixed at the Galactic column of $2.1 \times 10^{20} \text{ cm}^{-2}$ (Dickey & Lockman 1990, Murphy et al. 1996).

We started by fitting the EPIC-pn data, 4–10 keV only. Residuals to a simple power-law fit ($\chi^2/\text{dof} = 1515/999$) showed an obvious Fe $K\alpha$ emission line, but also some interesting structure near 6.0 keV; see Figure 2a. In our fits,

we tested two competing models that explain the emission features roughly equally well. As explained below, in both models, narrow emission features are detected at 6.40 keV and 7.37 keV (Fe $K\alpha$ and Ni $K\alpha$ respectively). The models differ in how emission near 6.0 keV is modeled: as a narrow Gaussian emission line, or as a relativistic diskline (hereafter “GA” and “DL” models).

We started with the former case. First, we included a Gaussian component at 6.40 keV to model the Fe $K\alpha$ line. In the best-fit “GA” model, the Fe $K\alpha$ line best-fit energy, intensity and EW were $6.403^{+0.011}_{-0.010}$ keV, consistent with neutral Fe. Its intensity and EW were $3.5 \pm 0.4 \times 10^{-5}$ ph cm $^{-2}$ s $^{-1}$ and 91 ± 10 eV, respectively. Its width σ was 65 ± 14 eV, which corresponds to a FWHM velocity of 7000 ± 1500 km s $^{-1}$.

Figure 3 shows contour plots resulting from adding a “sliding Gaussian” to the “power-law + Fe $K\alpha$ line” model to trace the emission residuals after the narrow Fe $K\alpha$ line was modeled. That is, we added a Gaussian with width σ fixed at 10 eV and searched over 4–9 keV in units of 0.1 keV, i.e., in steps smaller than the instrumental resolution. The narrow feature near 6.0 keV is clear; other residuals near 7.0 and 7.4 keV also warrant further investigation.

To model Fe $K\beta$ emission, we added a Gaussian to the model, keeping the energy centroid fixed and width σ tied to that of the Fe $K\alpha$ line. However, the line was not significantly detected according to an F -test. The upper limit to the line’s EW was 15 eV; the upper limit on the $K\beta/K\alpha$ normalization ratio was 0.19 (yielding no useful constraints on the ionization state of the Fe-line emitting material). We included this feature in the rest of the fits for completeness, with intensity fixed to 0.13 times that of the Fe $K\alpha$ line. Residuals to a model consisting of the power-law and the $K\alpha$ and $K\beta$ lines (where χ^2/dof was 1028.3/996) are plotted in Figure 2b.

We next added an Fe K edge at 7.11 keV (energy fixed) likely associated with reflection; χ^2/dof dropped to 1017.6/995; residuals to a model including the edge are plotted in Figure 2c. In the best-fit model, the optical depth τ was 0.05 ± 0.03 .

Next, we used a Gaussian component to model an emission line at $7.39^{+0.08}_{-0.07}$ keV, with width σ tied to that of the Fe $K\alpha$ line, consistent with emission from Ni $K\alpha$. Its intensity and equivalent width were $4^{+4}_{-3} \times 10^{-6}$ ph cm $^{-2}$ s $^{-1}$ and 13^{+13}_{-10} eV, respectively. χ^2/dof dropped to 1010.2/993; it was significant at 97.3% confidence according to an F -test to include this line. Residuals to a model including this line are plotted in Figure 2d.

Next, we added a narrow Gaussian emission profile near 6.0 keV to model those residuals; $\Delta\chi^2$ was -24.94 for 3 less dof , significant at $>99.99\%$ confidence according to a standard F -test. This line is not resolved (width $\sigma < 200$ eV). Its intensity and EW are $9^{+8}_{-4} \times 10^{-6}$ ph cm $^{-2}$ s $^{-1}$ and 21^{+19}_{-9} eV, respectively. A contour plot of intensity versus energy (confidence levels are for two interesting parameters) is shown in Figure 4. The best-fit line energy is $6.04^{+0.18}_{-0.04}$ keV inconsistent with 6.24 keV, the lowest photon energy associated with a Compton shoulder scattering feature. Using a Gaussian to model a Compton shoulder,

we should expect a centroid energy > 6.24 keV; fixing the Gaussian line energy at 6.24 keV failed to fully model away the 6.0 keV residuals. We performed Monte Carlo simulations to assess the statistical significance of this emission feature, as standard usage of the F -test may overestimate the statistical significance of lines at arbitrary energies such as this one (see e.g., warnings by Protassov et al. 2002). The simulations were conducted following §4.3.3 of Markowitz, Reeves & Braito (2006); see also §3.3 of Porquet et al. (2004). The simulations indicated that the likelihood that the 6.0 keV emission line is photon noise is $< 0.1\%$, i.e., the line is significant at $> 99.9\%$ confidence.

In this best-fit “GA” model, χ^2/dof was 983.2/990; Γ was 1.57 ± 0.03 . Other best-fit parameters are shown in Table 1. Residuals are plotted in Figure 2e.

Next, we tried to model the 6.0 keV feature as the red wing of a relativistic diskline profile. We used a LAOR model profile (Laor 1991) to model the diskline, with emissivity index β^{12} fixed at 3. χ^2/dof was 988.7/989 ($\Delta\chi^2 = -16.8$; significant at 99.8% confidence in an F -test) in the best-fit “DL” model. The EW of the diskline was 81^{+42}_{-30} eV; its inclination was $< 25^\circ$, and the inner radius was $< 22 R_g^{13}$. Visually, there still remained correlated, emission-like residuals from 5.9–6.1 keV, as shown in Figure 2f, which might at first suggest that the 6.0 keV emission feature may be better modeled as a narrow feature than as a red wing of a diskline. However, given the similar values of χ^2/dof and the instrument resolution, it would be difficult to demonstrate that the difference in residuals between the two models is not consistent with photon noise.

3.1. MOS 1+2 spectral fits to the Fe K bandpass

As a double-check on spectral modeling, we applied our best-fit “GA” model to both time-averaged MOS spectra (fit simultaneously, with all line parameters tied between both MOS spectra). The power-law indices and normalizations were allowed to differ between MOS 1 and MOS 2. Overall, the MOS and PN yielded qualitatively similar results. A simple power-law fit resulted in $\chi^2/dof = 771.9/558$; data/model residuals are plotted in the top panel of Figure 5. Adding Gaussian components to represent Fe $K\alpha$ and $K\beta$ emission in a manner similar to the pn fits caused χ^2/dof to drop to 546.86/555. Again we performed a “sliding narrow ($\sigma = 10$ eV) Gaussian” test; the resulting contours are plotted in Figure 6 and again indicate emission near 6.0–6.1 keV.

Finally, adding a narrow Gaussian (width σ fixed at 10 eV) at $6.11^{+0.06}_{-0.13}$ keV further improved the fit; χ^2/dof fell to 535.87/553 ($\Delta\chi^2 = -11.0$ for two less dof ; significant at 99.7% confidence according to an F -test used in the standard way). The best-fit values of the intensity and EW were $6.4 \pm 3.4 \times 10^{-6}$ ph cm $^{-2}$ s $^{-1}$ and 13 ± 7 eV, respectively. Data/model residuals for the best-fit model are plotted in the bottom panel of Figure 5 (There remain ~ 10 – 15% residuals in ratio space near 7.0 and 7.5 keV in Figure 5, but Figure 6 indicates that those features are not detected with high significance.). A contour plot of the intensity of the emission line at 6.11 keV versus line energy is plotted in Figure 7. Again we performed Monte Carlo simulations to gauge the detection significance, finding the

¹² radial emissivity per unit area is quantified as a power law, $r^{-\beta}$

¹³ $1 R_g \equiv GM_{BH}/c^2$

line to be detected at 95% confidence in the MOS 1+2 spectrum i.e., independent of the pn detection. In fact, we can multiply the independent null hypothesis probabilities for the pn and MOS (< 0.001 and 0.05) to yield a “effective” null hypothesis probability of $< 5 \times 10^{-5}$.

The detection of features at 6.0–6.1 keV in simultaneous pn and MOS 1+2 spectra illustrates the importance of observing with multiple X-ray instruments to attempt to distinguish between narrow and/or weak features which may be intrinsic to the target and features which are artifacts associated with photon noise (even when Monte Carlo simulations are used to gauge the detection significances in individual spectra). The likelihood that a strong emission feature could appear at the same energy in both the pn and the MOS 1+2 spectra and be due to photon noise is likely quite small.

The photon indices for the MOS 1 and MOS 2 spectra were 1.37 ± 0.04 and 1.46 ± 0.04 , respectively; the flatter values of the photon index compared to the pn are likely the result of pile-up (MOS spectra extracted using only pattern 0 events has photon indices which were ~ 0.3 steeper than the MOS pattern 0–12 spectra). Finally, we added an Fe K edge (energy fixed at 7.11 keV); χ^2/dof fell to 517.4/552 for $\tau = 0.09 \pm 0.04$. Emission from Ni K α was not significantly detected. All other parameters were consistent at the 90% confidence level with those measured by the pn.

We also applied the best-fit “DL” model to the MOS 1+2 spectrum. χ^2/dof was 504.9/550, with all diskline and Fe K α line parameters consistent with those in the pn fits.

4. EPIC PN BROADBAND SPECTRAL MODELING

We started with the best-fit “GA” model and included data down to 0.2 keV. In addition to the Galactic column, we included a ZWABS component at the systemic redshift to model any excess cold absorption associated with e.g., the host galaxy or circumnuclear material, $N_{H,local}$.

The residuals (Figure 8a) showed a large soft excess and a large absorption trough at ~ 0.73 to ~ 0.92 keV which we identify as an Fe UTA feature. A narrow absorption feature near 1.34 keV is apparent, likely due to Mg XI. A narrow absorption feature near 1.85 keV could be due to Si XIII, but could also be due to calibration uncertainties associated with the instrumental Si K edge.

We first modeled the soft excess using a steep power-law with photon index Γ_{SX} near 3. Our final, best-fit model (including modeling the warm absorbers and O VII emission line; see below) is henceforth referred to as the “SXPL (soft X-ray power law)” model. In the best-fit SXPL model, Γ_{SX} was $3.35^{+0.27}_{-0.10}$. We also added another layer of cold absorption at the systemic redshift, applying it only to the hard X-ray power law; in the best-fit SXPL model, its column density $N_{H,HX}$ was $2.9^{+0.3}_{-0.8} \times 10^{21} \text{ cm}^{-2}$. This improved the overall fit substantially (χ^2/dof fell to 3070.3/1730), but the 0.7–0.9 keV trough remained; see Figure 8b. In this model, Γ_{HX} was 1.64; we note that forcing the photon indices of the soft and hard power-law components Γ_{SX} and Γ_{HX} to be equal resulted in a very poor fit, with $\chi^2/dof = 6057/1731$.

Next, we used an XSTAR grid, which assumed a turbulent velocity width of 100 km s^{-1} , to model a layer of

warm absorption with ionization parameter $\log \xi$ and column density N_H . The grid assumed an underlying optical to X-ray spectral energy distribution described as follows: Below 0.001 keV, a power-law component with spectral index $\alpha = 1.0$ ($\Gamma = 2.0$); from 0.001 to 0.04 keV, a power law with $\alpha = 0.2$ ($\Gamma = 1.2$), following e.g., Elvis et al. (1994) and Netzer (1996); from 0.04 to 1.0 keV, a steep power law with $\alpha = 1.9$ ($\Gamma = 2.9$; the intrinsic EUV continuum is not well studied, but we assume that the soft excess seen in the *XMM-Newton* spectrum extends down to 0.04 keV); and above 1.0 keV, a power law with $\alpha = 0.5$ ($\Gamma = 1.5$), with the >0.04 keV power law indices based on the best-fitting SXPL model. Initially, solar abundances and a zero velocity offset relative to systemic were assumed. Applying one zone of warm absorption to the model, χ^2/dof fell to 2184.1/1728 for $\log \xi \sim 2.2$ and $N_H \sim 2 \times 10^{21} \text{ cm}^{-2}$. As shown in Figure 8c, however, significant data/model residuals remained. A model incorporating two zones of warm absorption successfully modeled all the absorption-like residuals, including the trough near 0.75 keV; χ^2/dof fell to 1942.1/1726. In this model, the two X-ray absorbers had ionization parameters $\log \xi_{lo}$ near 0.3 and $\log \xi_{hi}$ near 2.5. We henceforth refer to the two X-ray absorbers as the low-ionization X-ray absorber (though the ionization parameter is still higher than that of the optical/UV lukewarm absorber; see §9), and high-ionization X-ray absorber, respectively.

By now, the residuals (see Figure 8d) showed a narrow emission feature near 0.56 keV, likely due to O VII. Adding a narrow Gaussian component at 0.58 ± 0.01 keV with width σ fixed at 1 eV caused χ^2 to drop by 75 for two less *dof*. However, we note that the warm absorbers each predict narrow absorption lines due to O VII, so there are likely large systematic uncertainties associated with the measured intensity of the O VII emission line. This model, with $\chi^2/dof = 1866.9/1724$, is our best-fit SXPL model. In this model, the column densities and ionization parameters of the low- and high-ionization absorbers are: $N_{H,lo} = 1.0^{+0.3}_{-0.1} \times 10^{21} \text{ cm}^{-2}$, $\log \xi_{lo} = 1.45^{+0.16}_{-0.07}$, $N_{H,hi} = 1.8^{+1.2}_{-0.6} \times 10^{21} \text{ cm}^{-2}$, and $\log \xi_{hi} = 2.93^{+0.15}_{-0.09}$. Other best-fit parameters are listed in Table 2. The data/model residuals are shown in Figure 8e. Residuals near 1.8 and 2.2 keV are instrumental (Si K and Au M). Narrow emission-like features near 0.42 and 0.92 are tempting to identify as N VI and Ne IX emission, but they are likely narrower than the instrument resolution. There also appear to be some negative residuals near 6.8 keV, close to the energies associated with Fe XXV and Fe XXVI. However, fitting this feature with an inverted Gaussian does not yield significant improvement to the fit; it is likely a spurious feature and will not be discussed further.

Note that residuals near the expected O and Fe L3 edge energies due to dust (0.53 and 0.71 keV) are fine; we do not require additional edges at those energies (though we revisit this issue with the higher resolution RGS data below). If dust is present in the warm absorber, abundances of O and Fe (and also Si and C) may be expected to be low due to depletion onto grains (see Snow & Witt 1996). However, the measured O and Fe abundances of the warm absorber are consistent with solar, and left fixed at solar values for the remainder of the paper.

In the best-fit SXPL model, the hard X-ray power-law

component has a photon index $\Gamma_{\text{HX}} = 1.57 \pm 0.02$, a couple tenths lower than “canonical” values of 1.8–1.9 in many broad-line Seyferts. We therefore explored the possibility that the observed low value of the photon index is an artifact caused by a yet-unmodeled partial-covering absorbing component with column density $N_{\text{H,PC}} \sim 10^{23} \text{ cm}^{-2}$ along the line of sight to the nucleus. Such material is expected to exist within light-days of the black hole, as demonstrated by the 2000-1 obscuration event. Furthermore, such a column is required to explain the origin of the Fe K α line (see §9.4) in the absence of strong Compton reflection (see §6). Modifying the hard X-ray power-law component to be absorbed by a partial-covering neutral absorber with $N_{\text{H,PC}}$ set to 0.3, 1.0 or $3.0 \times 10^{23} \text{ cm}^{-2}$, we find only upper limits to the covering fraction in the range 5–15%. In the best fit models, Γ_{HX} was never higher than about 1.6. Partial-covering models are not analyzed further.

As before, we applied our best-fit SXPL model to the time-averaged MOS 1+2 spectra as a double-check. The MOS fits, using this model and fitting over 0.4–10 keV, and allowing power-law component parameters to differ between MOS 1 and MOS 2, yielded $\chi^2/dof = 1406.33/1017$, and required slightly higher values of the column density and ionization parameter of the high-ionization warm absorber ($N_{\text{H,hi}} = 1.2_{-0.5}^{+0.3} \times 10^{21} \text{ cm}^{-2}$ and $\log \xi_{\text{hi}} = 3.22_{-0.11}^{+0.04} \text{ erg cm s}^{-1}$, respectively) compared to the pn. Γ_{SX} for MOS1 and MOS2 were consistent with that for the pn. Γ_{HX} for MOS1 was 1.52 ± 0.01 , slightly flatter than that for the pn. Γ_{HX} for MOS2 was 1.57 ± 0.02 , consistent with the pn. All other parameters were consistent at the 90% confidence level with those measured by the pn.

4.1. Alternate parametrizations of the soft excess

We returned to the pn data to consider alternate methods of modeling the soft excess. An alternate parametrization of the soft excess, a blackbody, yields a nearly identical value of χ^2/dof (1870.4/1724). Data/model residuals are plotted in Figure 8f. The blackbody temperature $k_{\text{B}}T = 83_{-4}^{+1} \text{ eV}$ in the pn fit ($77 \pm 3 \text{ eV}$ for the MOS), similar to values found for model fits incorporating blackbody components for most other Seyferts, e.g., $k_{\text{B}}T \sim 100\text{--}150 \text{ eV}$ for many narrow-line Seyfert 1s. It is generally accepted now that a blackbody is a physically unphysical description of the soft excess in AGN. Bechtold et al. (1987) were the first to point out that the best-fit blackbody temperatures are generally too high to be associated with accretion disks around supermassive black holes. The consistency of blackbody temperatures across a wide range of Seyfert 1 properties, including black hole mass, further suggests that a blackbody is an unphysical parametrization (e.g., Gierliński & Done 2004). However, the best-fit blackbody temperature in the current fit is consistent with previous results for NGC 3227 (e.g., Komossa & Fink 1997b). We note that in this model (henceforth denoted simply as the “BB” model), $N_{\text{H,HX}}$ has dropped to $\leq N_{\text{H,local}}$, i.e., the value of $N_{\text{H,HX}}$ is model dependent.

We next tried fitting the soft excess using the Comptonization model COMPST (Sunyaev & Titarchuk 1980). Such components have been used e.g., by Gierliński & Done (2004) to model the soft excess emission as Comptonization of accretion disk seed photons in a cool

($k_{\text{B}}T \sim 0.3 \text{ keV}$), optically-thick corona, distinct from the optically-thin, hot ($k_{\text{B}}T \sim 100 \text{ keV}$) corona generally thought to be responsible for the hard X-ray power-law component in Seyferts. Physically, such a component could be potentially associated with the transition region between an optically-thick accretion disc and an optically-thin inner corona (Magdziarz et al. 1998), or in the hot, ionized surface of the accretion disk (Hubeny et al. 2001; Janiuk, Czerny & Madejski 2001). However, similar to the blackbody component, using such Comptonization components to model soft excesses tends to yield a narrow range of best-fit temperatures across a range of Seyfert properties. In our best-fit model (“COMPST”, where $\chi^2/dof = 1863.4/1723$), $k_{\text{B}}T = 0.35_{-0.03}^{+0.02} \text{ keV}$, and optical depth $\tau = 24_{-4}^{+2}$, similar to previous fits to other AGN (however, see e.g., Vaughan et al. 2002 for warnings regarding the covariance of optical depth and temperature in this model). Best-fit parameters for the models using the blackbody and COMPST components are listed in Table 2, though the reader must bear in mind the difficulties each of these models faces in terms of physical plausibility. Data/model residuals are not plotted, as they are virtually identical to those for the SXPL model (Figure 8e).

Figure 9 shows unfolded model spectra for the SXPL, BB and COMPST models, demonstrating how the steep soft excess is produced in each (and demonstrating why the value of $N_{\text{H,HX}}$ depends on how the soft excess is modeled).

Many recent forays into modeling soft excesses have found success using ionized reflection models modified by relativistic smearing, i.e., a blurred ionized reflector (e.g., Crummy et al. 2006); an origin in atomic features could plausibly explain the consistency of soft excess features across a range of Seyfert black hole masses. Starting with the best-fit SXPL model, we removed the soft X-ray power-law and the 6.04 keV emission line, and added a Ross & Fabian (2005) reflection component convolved with the kernel associated with relativistic motion around a Kerr black hole (a LAOR profile). The photon index of the illuminating continuum was tied to that of the hard X-ray power-law. The disk outer radius was fixed at $400 R_{\text{g}}$; the emissivity index was fixed at 3. The 6.4 keV Fe K α and Ni K α line parameters were fixed at the values in the time-averaged spectrum. The best-fit model had $\chi^2/dof = 2698.4/1721$, with large ($\pm 10\%$) correlated residuals below $\sim 2 \text{ keV}$ (see Figure 8g). The best-fit Fe abundance was < 0.15 , and the best-fit value of the reflector ionization parameter ξ pegged at the lower limit of 30 erg cm s^{-1} , likely indicating that lower values of ξ may be more appropriate. The low level of Compton reflection $> 10 \text{ keV}$ in NGC 3227, $R \lesssim 0.5$, as demonstrated in §6, also suggests that ionized reflection in NGC 3227, if it exists, is not strong. We do not consider this model further.

Finally, we tried to model the soft excess using smeared absorption to model ionized absorbing material moving at relativistic velocity, such as a wind launched from the inner accretion disk SWIND1 (Gierliński & Done 2006). Assuming a single power-law to model the intrinsic continuum emission, modified by smeared absorption, yielded a poor fit ($\chi^2/dof = 8388/1728$). Modeling the intrinsic continuum using two power-laws, as in the SXPL model, and adding smeared absorption plus the low-ionization X-ray absorber, yielded a good fit ($\chi^2/dof = 1892/1723$),

in which a smeared ionized absorber with $\log \xi \sim 2.7$ erg cm s $^{-1}$ was able to mimic the high-ionization X-ray absorber, given the resolution of the pn. However, analysis of the RGS spectrum (§5) supports the need for both the low- and high-ionization X-ray absorbers, and so we do not consider this model further.

5. RGS MODELING OF THE IONIZED ABSORBERS AND EMISSION LINES

We first modeled the continuum of the RGS spectrum with a model of the same form as the SXPL model from the pn fits: a steep soft power-law with $\Gamma_{\text{SX}} \sim 3.2$ absorbed by a cold column $N_{\text{H,local}} = 1 \times 10^{21}$ cm $^{-2}$, and a hard power-law absorbed by a column $N_{\text{H,HX}} \sim 1 \times 10^{22}$ cm $^{-2}$, and dominating the continuum only above ~ 1.5 keV (and with both $N_{\text{H,HX}}$ and Γ_{HX} very poorly constrained, given that the RGS only covers up to 2 keV). The residuals to this model ($\chi^2/\text{dof} = 1156/433$) are shown in Figure 10.

There is a broad absorption feature at ~ 740 – 780 eV, which we identify as an Fe M-shell UTA trough. Its energy range (assuming a velocity offset from systemic near zero) indicates that $\log \xi$ of the gas where this feature originates must be in the range $\sim +0.3$ to $+1.4$, according to an XSTAR table; and absorption is mainly due to species of Fe in the ionization range $\sim \text{VI}$ – XIII , and likely not due to Fe $\sim \text{XIV}$ – XVI (Gu et al. 2006).

Many narrow absorption features are evident; the tentative identifications (and lab-frame energies) of the most visually prominent ones are labeled in Figure 10 and include C VI Ly α (368 eV), C VI Ly β (436 eV), N VII (500 eV), O VIII Ly α (653 eV), O VII He β (666 eV; perhaps blended with the N VII edge), O VII He γ (698 eV), Fe XVII 3d–2p (812 eV), Ne IX (922 eV, though this line may be blended with Fe absorption lines at ~ 918 – 934 eV), Ne X (1022 eV) and Mg XI (1352 eV).

A strong edge at 739 eV due to O VII is not obvious, though it could be blended with the Fe UTA feature. Similarly, an edge at 870 eV due to O VIII is not obvious. The lack of a very strong ($\gtrsim 20$ – 30% drop) O VIII edge suggests that any absorbing material containing O VIII has a hydrogen column density $N_{\text{H}} < 10^{22.5}$ or so. There are also narrow emission features near the energies for the O VII and N VI resonance lines (574 eV and 428 eV, lab-frame); these are discussed further below.

We next modeled the two ionized X-ray absorbers discussed in the pn fits above, using the same XSTAR table models, with their respective velocity offsets relative to systemic initially frozen at zero, and with abundances fixed to solar values. χ^2/dof fell to 955.40/429 for values of $\log \xi_{\text{lo}}$ and $\log \xi_{\text{hi}}$ near 1.2 and 2.8, respectively, and with column densities for each near 1×10^{21} cm $^{-2}$. However, many of the absorption lines seemed to be blueshifted slightly.

We tried various combinations of allowing the absolute redshift of each absorber, z_{lo} and z_{hi} , to be thawed from the systemic value. Thawing z_{hi} only yielded $\chi^2/\text{dof} = 884.87/428$ for a best-fit value of z_{hi} near -0.0036 (-0.0075 relative to systemic). Thawing both z_{hi} and z_{lo} , but keeping their values tied, yielded $\chi^2/\text{dof} = 887.46/428$ for a best-fit value of $z_{\text{hi}} = z_{\text{lo}} = -0.0033$ (-0.0072 relative to systemic). Finally, thawing both z_{hi} and z_{lo} and allowing them to vary independently, yielded $\chi^2/\text{dof} = 864.09/427$

for best-fit values of $z_{\text{hi}} = -0.0034$ (-0.0073 relative to systemic) and $z_{\text{lo}} = +0.0016$ (-0.0023 relative to systemic).

Finally, to this last model (which had the lowest χ^2 value), we added five narrow (width $\sigma = 0.5$ eV) Gaussian components to represent emission at the systemic redshift from the O VII (f), (i) and (r), N VII, and N VI (r) (note that we model the sum of the two intercombination lines for O VII). Their measured energies, intensities, and fit parameters are listed in Table 3. N VI (f) and N VI (i) emission lines were detected only as upper limits, with intensities $< 6.7 \times 10^{-5}$ and $< 3.0 \times 10^{-5}$ ph cm $^{-2}$ s $^{-1}$, respectively, and so are not listed in Table 3. However, as for the pn fits, we caution that since both warm absorbers require some O VII, N VI and N VII absorption, the emission line intensities likely have large systematic uncertainties. Final parameters for the ionized absorbers in our best-fit SXPL model (with $\chi^2/\text{dof} = 785.7/417$) are $\log \xi_{\text{lo}} = 1.21^{+0.18}_{-0.08}$, $N_{\text{H,lo}} = 1.1^{+0.1}_{-0.2} \times 10^{21}$ cm $^{-2}$, $\log \xi_{\text{hi}} = 2.90^{+0.21}_{-0.26}$, and $N_{\text{H,hi}} = 2.4^{+2.0}_{-1.2} \times 10^{21}$ cm $^{-2}$; other model parameters are listed in Table 4. We note that $\Gamma_{\text{SX}} = 3.00 \pm 0.25$ and $N_{\text{H,local}} = 10.5^{+1.2}_{-1.9} \times 10^{20}$ cm $^{-2}$, both consistent with the best-fit SXPL model for the EPIC data.

In this model, the best-fit value for the redshift of the high-ionization absorber is z_{hi} (absolute) $= -0.00302^{+0.00057}_{-0.00080}$ or z_{hi} (relative to systemic) $= -0.00688^{+0.00057}_{-0.00080}$, which corresponds to an outflow velocity of $-(2060^{+240}_{-170})$ km s $^{-1}$ relative to systemic. For the low-ionization absorber, z_{lo} (absolute) $= +0.00246^{+0.00144}_{-0.00064}$ or z_{lo} (relative to systemic) $= -0.00140^{+0.00144}_{-0.00064}$, corresponding to an outflow velocity of $-(420^{+430}_{-190})$ km s $^{-1}$ relative to systemic. Given the best-fit values of the two warm absorbers here and the relative line strengths expected in those cases, the outflow velocity for the high-ionization absorber is constrained primarily by the narrow absorption lines due to Ne IX, Ne X, and Mg XI; constraining the respective energies of each of these lines separately yielded corresponding outflow velocities relative to systemic of 1300^{+650}_{-300} , 600 ± 600 , and 1800 ± 600 km s $^{-1}$, respectively. Isolating the observed C VI Ly β , N VII and O VIII Ly α absorption lines yielded similar velocity offsets (2700 ± 700 , 1800 ± 600 and 1840 ± 460 , respectively), though contributions to these lines from both the low- and high-ionization absorber are expected, given the best-fit ionization levels. The only strong absorption features which are unique to only the low-ionization absorber and unambiguously studied here are the (possibly blended) Fe UTA feature and the O VII edge. Models wherein the outflow velocity of the low-ionization absorber is either much closer to systemic, equal to that of the dusty lukewarm UV absorber (tens of km s $^{-1}$; Crenshaw et al. 2001), or equal to that of the high-ionization absorber are not definitively ruled out at high confidence. Setting the absolute value of z_{lo} equal to systemic, $+0.00353$ (-0.00033 relative to systemic, corresponding to an outflow velocity of 100 km s $^{-1}$), or z_{hi} or $+0.003859$ and refitting yielded increases in χ^2 of only 9, 6, and 16 respectively. In each case, the outflow velocity for the high-ionization absorber remained virtually unchanged from the best-fitting SXPL model.

As an additional confirmation on the XSTAR table results, we measured the *EWs* of selected individual ab-

sorption features. The measured EW for the Fe UTA (-13_{-8}^{+4}) eV is consistent with the prediction from an XSTAR table with $N_{\text{H,lo}} = 1.1 \times 10^{21} \text{ cm}^{-2}$ and $\log \xi_{\text{lo}} = 1.21$. The measured EW s for Ne IX (-5.5 ± 2.0 eV), Ne X (-4.4 ± 1.6 eV) and Mg XI (-4.1 ± 2.0 eV) are in good or reasonable agreement (given the data quality) with the predicted EW s from an XSTAR table with $N_{\text{H,hi}} = 2.4 \times 10^{21} \text{ cm}^{-2}$ and $\log \xi_{\text{hi}} = 2.90$ (these lines are not expected to be generated with significantly noticeable EW in the low-ionization absorber). The measured EW s for C VI Ly β (-1.0 ± 0.9 eV), N VII ($-(1.1_{-0.2}^{+1.3})$ eV) and O VIII (-3.3 ± 0.7 eV) are in good or reasonable agreement (given the data quality) with the sums of the predicted EW s from the two XSTAR tables.

Most of the remaining data/model residuals are consistent with RGS calibration uncertainties or are instrumental in nature (Pollack et al. 2007; observed energies listed): a small dip near 394 eV; large residuals near the O instrumental edge, 524–530 eV; a small dip at 573–577 eV (which further adds to the systematic uncertainties associated with O VII emission lines intensity); residuals at ~ 680 –695 eV, associated with an instrumental fluorine feature; an apparent edge at 850 eV; and a dip at 937–943 eV. Many of these instrumental features are also seen in other RGS spectra of Seyferts (e.g., Braito et al. 2007).

We rely on the RGS primarily for determination of warm absorber and soft X-ray emission line parameters; all hard X-ray parameters are best constrained by the EPIC data. Still, for the SXPL model, most best-fit parameters (including those for the warm absorbers) were consistent at the $\Delta\chi^2 = 2.71$ significance level between the RGS and the pn; $N_{\text{H,HX}}$ and Γ_{HX} were the exceptions, and clearly better constrained by the EPIC. Simultaneous RGS/pn fitting using the SXPL model ($\chi^2/\text{dof} = 3220/2161$) yielded best-fit values for Γ_{SX} , $N_{\text{H,local}}$ and warm absorber column densities and ionization parameters consistent with those measured by the RGS and EPIC-pn separately. Similarly, modeling the continuum in the RGS data using a blackbody or a COMPST component yielded good fits ($\chi^2/\text{dof} = 805.7/417$ and $806.4/416$, respectively), with a best-fit blackbody temperature and COMPST parameters consistent with those measured using only EPIC data, and with no significant changes to the warm absorber or emission line parameters compared to using a soft power-law component to model the soft excess.

To this point, we have been assuming that the ionized absorbers along the line of sight have been full-covering. Using the RGS data, we tested a model wherein only a fraction of the continuum radiation is absorbed by the ionized absorbers. We found the upper limit to the fraction of continuum radiation that remains unattenuated by ionized absorption to be 30%, i.e., a covering fraction of $> 70\%$ for the RGS data. For the pn data, the covering fraction is inferred to be $> 93\%$.

We also tested for the presence of radiative recombination continuum (RRC) features in the RGS data associated with H- or He-like ions, expected if the emission lines are associated with gas that is photo-ionized. Using a REDGE component in XSPEC with energy fixed and with $k_{\text{B}}T$ fixed at 0.5 keV (arbitrary value), we found upper limits in the range 5–8 eV for C V, C VI, N VI and O VII RRCs, upper limits ≤ 20 eV for O VIII and Ne IX, and an upper limit

near 50 eV for an Ne X RRC. A N VII RRC at 667 eV significantly improved the fit, but that was due to fitting the instrumental fluorine feature, and therefore is likely not real. Finally, we note no significant emission from the Fe XVII L line (3d–2p) at 826 eV (upper limit of 1 eV), limiting the possibility that the observed emission lines are generated via collisional ionization processes.

We now discuss the search for X-ray spectral features in the RGS associated with dust embedded in the warm absorbers. The expected effects of embedded dust on the X-ray spectrum are: 1) Edges due to neutral Fe, O, C, Si and Mg (depending on dust composition) in excess from the absorption expected from gas. The O edge would be at 531 eV. The three Fe edges are the L3, L2, and L1 edges, at 707, 721 and 846 eV (assuming oxidized Fe; edges due to pure Fe would be ~ 3 eV higher), roughly in a 10:5:1 ratio (e.g., Kortright & Kim 2000; Bearden & Burr 1967; Schulz et al. 2002). 2) There may be weak, narrow absorption lines due to Fe oxide species, in particular at 702 eV (e.g., Crocombette et al. 1995). 3) Fe, C and O abundances in the warm absorber would be low due to depletion onto dust grains (Snow & Witt 1996; Komossa & Fink 1997a).

Near 707 eV and 721 eV (the Fe L3 and Fe L2 edge energies) the residuals in the RGS spectrum of NGC 3227 do not appear obviously edge-like. Inserting an edge at any of neutral Fe or O energies does not improve the fit; upper limits to the optical depths of O, Fe L3 and Fe L2 in excess of the neutral absorption associated with the gas components modeled above (both local and Galactic) are 0.17, 0.05 and 0.21, respectively. In contrast, the Fe L3 edges seen in Cyg X-1 (Schulz et al. 2002) and MCG-6-30-15 (Lee et al. 2001) with the *Chandra* HETGS are both $\gtrsim 50\%$ drop across the edge ($\tau \gtrsim 0.7$). From the Fe L3 edge in NGC 3227, the implied upper limit on the Fe I column density is $\sim 10^{17} \text{ cm}^{-2}$. Assuming the abundances of Lodders (2003), the corresponding equivalent hydrogen column density is constrained to be less than $\sim 10^{21.5} \text{ cm}^{-2}$. This limit is consistent with the equivalent hydrogen column density implied by optical line absorption (see §1). The limit on the EW (relative to locally-determined and unabsorbed continuum) of a narrow (width $\sigma = 0.5$ eV) absorption line at 702 eV is -0.5 eV. Finally, thawing the abundances of Fe, O, and Mg in the warm absorbers (abundances in both absorbers tied) does not yield significant evidence for deviations from solar abundances.

6. CONSTRAINING THE >10 KEV CONTINUUM WITH RXTE AND SWIFT-BAT

We fit archival *RXTE* data and *Swift* Burst Alert Telescope (BAT) 9-month survey data to constrain the amount of the Compton reflection and constrain any high-energy power-law cutoff. We did not do simultaneous fitting with the EPIC spectrum, since the *XMM-Newton* and latest *RXTE* and BAT data obtained were separated by a year and since the only two broadband model components in the range of overlap are the variable hard X-ray power-law and the hard X-ray absorber, whose column $N_{\text{H,HX}} \lesssim 10^{21} \text{ cm}^{-2}$ is not well constrained by the PCA. However, the observed 2–10 keV flux during the 2006 *XMM-Newton* observation, $F_{2-10} = 3.5 \times 10^{-11} \text{ erg cm}^{-2} \text{ s}^{-1}$, fell in the approximate range probed by the *RXTE* monitoring; only during MJD ~ 51850 –52050 was F_{2-10} observed to be con-

sistently below 2×10^{-11} erg cm $^{-2}$ s $^{-1}$. This suggests that *XMM-Newton* caught the source in a “typical” flux state.

We fit the PCA data over the 3.3–30 keV range; the source is not well detected at higher energies. HEXTE data below 24 keV were ignored as the responses of clusters A and B diverge somewhat for faint sources (N. Shaposhnikov, private communication, 2005); there is good agreement above this energy. HEXTE data above 100 keV were also ignored. 14–195 keV BAT data were included; four-channel spectra and response matrices were taken from the BAT 9-month AGN catalog website¹⁴. A constant coefficient was included in all spectral models to account for minor normalization offsets between the PCA and HEXTE; its value for the HEXTE spectra relative to the PCA spectrum was typically 0.8–0.9. No constant was needed for the BAT spectrum relative to the PCA spectrum.

We applied a model consisting of a power-law (initially with a high-energy cutoff set arbitrarily at E_c 500 keV), a Gaussian emission line at 6 keV to model Fe K α emission, and a component to model Compton reflection from neutral material, using PEXRAV (Magdziarz & Zdziarski 1995), all modified by a cold column $N_{H,HX}$ constrained to be less than 6×10^{21} cm $^{-2}$. The PEXRAV component’s inclination was fixed at 45°, solar Fe abundances were assumed, and the high energy cutoff was tied to that of the power-law. The best-fit model had $\chi^2/dof = 297/111$, the photon index Γ_{HX} was 1.66 ± 0.01 , and the value of the Compton reflection strength R ¹⁵ was $0.16^{+0.08}_{-0.02}$. Allowing the high-energy cutoff to be free and re-fitting, χ^2/dof fell to 222/110 (significant at 5.6σ confidence according to an F -test). Γ_{HX} was 1.63 ± 0.02 , R was 0.40 ± 0.07 , and $E_c = 90 \pm 20$ keV. The cold column $N_{H,HX}$ was $6.0^{+0}_{-0.8} \times 10^{21}$ cm $^{-2}$ (uncertainty pegged at upper limit). The residuals to the best-fit models with and without a high-energy cutoff are shown in Figure 11¹⁶.

Because the *RXTE* and *XMM-Newton* observations were not simultaneous, it is not clear whether the slightly flatter value of Γ_{HX} for the pn in the SXPL model (1.57 ± 0.02) compared to that for the time-averaged *RXTE* spectrum is due to source variability or associated with systematic differences in modeling spectra taken with two instruments with very different energy resolution. For example, the average Fe K α line flux as measured by the PCA was $9 \pm 1 \times 10^{-5}$ ph cm $^{-2}$ s $^{-1}$, but this is not automatically an indication of line variability between the *RXTE* and *XMM-Newton* observations given the differences in PCA and EPIC resolution, the systematic uncertainties associated with fitting such a complex model to the low-resolution PCA data, and possible uncertainties associated with PCA/pn cross-calibration. All uncertainties listed here are one-dimensional statistical errors only and do not account for systematic uncertainties associated with correlations between parameters or for systematic instrumental uncertainties associated with observing faint objects. However, we can safely conclude that the

value of R must be relatively low: Figure 12 shows contour plots for E_c and R as a function of Γ_{HX} from the joint *RXTE*+*Swift*-BAT fit, demonstrating that values of $R > 0.6$ are rejected at high confidence.

7. TIME- AND FLUX-RESOLVED SPECTRAL FITS

We investigated the temporal behavior of the X-ray spectrum of NGC 3227 on a range of time scales. Any rapid variation in ionization parameter would rule out models where the warm absorber is spatially extended and/or located very far from the black hole; tracking ionization responses to continuum flux variations can yield constraints on the location of the warm absorbers (e.g., Krongold et al. 2007). Similarly, any rapid variation in the strength of an Fe K emission feature (e.g., Tombesi et al. 2007) would suggest an origin close to the X-ray illuminating source. We used the *XMM-Newton* spectrum to study variability on time scales $\lesssim 1$ day (hereafter “short” time scales); we used the *RXTE* intensive monitoring from 2000 April to June to investigate variability on time scales from ~ 2 weeks to 2 months (hereafter “medium” time scales), and the 1999–2005 monitoring to investigate variability on time scales from months to several years (“long” time scales”).

7.1. *XMM-Newton* time-resolved spectral fits

We investigated the <1-day time-resolved spectral behavior of NGC 3227 during the *XMM-Newton* observation by first splitting the EPIC-pn data into five segments of equal duration (good exposure time 18 ks); shorter durations would not have yielded adequate photon statistics in narrow features. In the Fe K bandpass, spectral fitting revealed several “candidate” narrow transient emission features between 4.5 and 5.2 keV, each with $\Delta\chi^2$ in the range -11 to -14 . Monte Carlo simulations (see §3) showed that each of these emission features were significant at 92–97% confidence. However, when one takes into consideration the number of segments searched over (Vaughan & Uttley 2008), the significance levels drop to 60–85% confidence; these features are not discussed further. Considering the broadband spectrum, all parameters for the neutral and ionized absorbers and the O VII emission line were consistent with those found in the time-averaged spectrum. Similarly, flux-resolved spectral analysis, performed on high- and low-flux pn spectra (extracted above and below a 0.2–12 keV pn count rate of 11.0 ct s $^{-1}$, respectively), yielded no significant evidence for variability of the neutral or ionized absorbers, the 6.4 keV Fe K α line, or the O VII line. The 6.04 keV line was not significantly detected with these short exposures.

However, we noticed in these time-resolved fits that the normalization of the soft excess increased by $\sim 25\%$ from the first 20 ks segment to the second segment. Similar results were obtained when modeling the soft excess as a steep power-law, a blackbody, or a COMPST component.

The rapid (ks and shorter) variations seen simultaneously in both the hard and soft X-ray light curves (Figure

¹⁴ <http://swift.gsfc.nasa.gov/docs/swift/results/bs9mon/>

¹⁵ $R \equiv \Omega/2\pi$, where Ω is the solid angle subtended by the reflector

¹⁶ The presence of the high-energy cutoff is also inferred from fitting PCA+HEXTE only: excluding the BAT data, and refitting, we find that including a high-energy cutoff still significantly improves the fit, with best-fit values consistent with the PCA + HEXTE + BAT fit, though the statistical uncertainty on E_c is 1.8 times larger. Ignoring the HEXTE data, and fitting PCA + BAT only, the best-fit values of Γ_{HX} , R , and E_c are $1.62^{+0.02}_{-0.04}$, $0.53^{+0.19}_{-0.08}$ and 65^{+10}_{-25} keV, respectively.

1) are similar to those routinely detected in other Seyferts; the associated variability mechanisms will be explored in depth in a future paper (Arévalo et al., in prep) and are not discussed further here. Here, we are concentrating on the soft X-ray band's relatively slower and distinct trend. Since this trend occurs over tens of ks, we will refer to it as "rapid" for the remainder of this paper.

We repeated the time-resolved analysis, dividing the data into ten segments of equal duration (9 ks good exposure time), fitting the SXPL model, and keeping all warm and cold absorber, O VII line and Fe emission line parameters frozen at their time-averaged values.

The resulting light curves of Γ_{HX} , Γ_{SX} and the normalizations of the SXPL and HXPL components are plotted in Figure 13. The SXPL normalization seems to track the light curve of 0.2–1 keV flux in Figure 1. To further illustrate the rapid variability of the soft excess, the data for segments 1 (the lowest soft excess flux bin), 2, and 6 (the highest soft excess flux bin) are plotted in Figure 9.

Finally, fractional variability amplitudes (F_{var} see Vaughan et al. 2003 for a definition) were calculated for 16 energy bands. The resulting F_{var} for the entire duration, for the first 20 ks, and for the final 80 ks are plotted in Figure 14, further illustrating the rapid variability in the soft excess. Further detailed variability analysis of the variable X-ray continuum, including coherence, intra-X-ray time lags and power spectral density function measurement, will be presented in a future paper (Arévalo et al., in prep).

7.2. *RXTE* time-resolved spectral fits

Time-resolved spectral fitting of the *RXTE* data closely followed Markowitz, Edelson & Vaughan (2003). Bin sizes were chosen to optimize the trade off between minimizing the uncertainties on Fe line flux and maximizing the number of bins. This yielded 5 bins, each of duration 13 days, for the medium time scale. On the long time scale, start/stop times were chosen to avoid 60-days gaps where *RXTE* did not observe the source due to sun-angle constraints, with most durations roughly 100 days before loss of PCU0 on 2000 May 12, and 150 days afterward, yielded 16 bins. Response matrices were generated separately for each segment.

We used a model consisting of a power law component, a Gaussian component to model Fe K emission, and a PEXRAV component to model Compton reflection, all absorbed by cold material (with a column density $N_{\text{H,HX}}$ constrained to be $< 6 \times 10^{21} \text{ cm}^{-2}$, unless the bins included data taken during the 2000-1 obscuring event). In the best fit models, the best-fit values of R , Fe line rest-frame energy centroid, and Fe line width σ were $0.4^{+0.2}_{-0.1}$ (0.2 ± 0.1), $6.26^{+0.10}_{-0.11}$ ($6.27^{+0.05}_{-0.04}$) keV, and $0.50^{+0.32}_{-0.14}$ ($0.33^{+0.09}_{-0.08}$) keV in the medium (long) time scale fits, respectively. To determine which parameters to leave free during each time-resolved fit, we first fit all segments simultaneously with all parameters tied, and thawed one parameter at a time, testing for significant improvement in the fit according to an F -test. We found it was significant to thaw the power law normalization, Γ_{HX} , Fe line intensity $I_{\text{FeK}\alpha}$, and $N_{\text{H,HX}}$ in the individual, time-resolved fits.

Errors for $I_{\text{FeK}\alpha}$ and Γ_{HX} were derived using the point-to-point variance¹⁷. Errors on values of F_{2-10} within a time bin were determined from the 2–10 keV continuum light curve, using the mean flux error on the ~ 1 ks exposures in that time bin. Figure 15 shows the resulting light curves for F_{2-10} , $I_{\text{FeK}\alpha}$, and Γ_{HX} .

Fractional variability amplitudes F_{var} were calculated. For the medium time scale, F_{var} for the F_{2-10} and $I_{\text{FeK}\alpha}$ light curves were $38.4 \pm 0.3\%$ and $22.7 \pm 10.3\%$, respectively, although we caution that with only 5 data points, these measured values of F_{var} are likely not highly reliable. For the long time scale, F_{var} for F_{2-10} and $I_{\text{FeK}\alpha}$ were $32.7 \pm 0.7\%$ and $20.0 \pm 4.3\%$. Qualitatively, these results are consistent with what Markowitz, Edelson & Vaughan (2003) found for a small sample of Seyferts: the Fe line does not vary as strongly as the continuum flux.

Inspection of the F_{2-10} and $I_{\text{FeK}\alpha}$ light curves would seem to indicate, to the human eye at least, similar variability trends. However, with so few points (especially for the medium time scale), such a statement is not highly significant. On the medium time scale, the best-fit linear relation is $I_{\text{FeK}\alpha} = 2.05 \pm 1.31 \times F_{2-10} + 4.1 \pm 3.1$, with $I_{\text{FeK}\alpha}$ in units of $10^{-5} \text{ ph cm}^{-2} \text{ s}^{-1}$ and F_{2-10} in units of $10^{-11} \text{ erg cm}^{-2} \text{ s}^{-1}$. Figure 16 shows the zero-lag correlation plot of $I_{\text{FeK}\alpha}$ as a function of F_{2-10} , with the best-fit linear relations plotted as dashed lines. The zero-lag Spearman rank correlation coefficient¹⁸ is 0.700; the corresponding null hypothesis probability (the probability that the correlation could arise from randomly chosen data points) is 16%; i.e., the correlation is significant only at 84% confidence.

For the long time scale data, the best-fit linear relation is $I_{\text{FeK}\alpha} = 1.44 \pm 0.30 \times F_{2-10} + 3.5 \pm 1.2$. The zero-lag Spearman rank correlation coefficient is $r=0.739$, significant at 99.6% confidence. We searched for lags using an Interpolated Cross Correlation Function (ICF; Gaskell & Peterson 1987, White & Peterson 1994), with errors determined using the bootstrap method of Peterson et al. (1998). The ICF peak correlation coefficient $r_{\text{max}}=0.854$ was reached at a delay of 75 ± 690 days (F_{2-10} leading $I_{\text{FeK}\alpha}$), i.e., consistent with zero lag.

With such few data points and low correlation coefficients on both medium and long time scales, any claim of a correlation must be deemed tentative at best. Cross correlation analysis is further complicated by the red-noise nature of the continuum (and likely line) light curves. Specifically, cross-correlation between two unrelated red-noise light curves can randomly yield spurious correlations with higher than expected values of the correlation strength r_{max} (e.g., Welsh 1999). Lags where r_{max} is not very close to 1.0 should thus be treated with skepticism. Additional monitoring, spanning much longer durations and wider ranges in both F_{2-10} and $I_{\text{FeK}\alpha}$ and encompassing additional upward/downward trends in the light curves of both F_{2-10} and $I_{\text{FeK}\alpha}$ are required to critically test for any significant correlation. We therefore conclude that there is, at best, tentative evidence from the *RXTE* time-resolved spectral fits for a significant fraction of the the Fe line intensity to respond to continuum variations on time scales shorter than 700 days. The lack of strong

¹⁷ See §3.3 of Markowitz, Edelson & Vaughan (2003) for further details and the definition of the point-to-point variance

¹⁸ calculated at <http://www.wessa.net/rankcorr.wasp>

hard X-ray variability during the *XMM-Newton* observation ($F_{\text{var}} = 8.5 \pm 0.2\%$ for the 3–10 keV light curve, binned to 600 s) means we cannot draw any conclusions about the response of the line on $\lesssim 1$ day time scales.

8. X-RAY/UV CONTINUUM LIGHT CURVE CORRELATIONS

The OM light curve of NGC 3227 displayed in Figure 1 shows a $\sim 10\%$ increase across the observation, with an RMS of 2.8%. Rapid optical/UV variability in Seyferts on time scales of $\lesssim 1$ day is relatively rare. Of the sample of 8 Seyferts examined by Smith & Vaughan (2007), NGC 3783 displayed the strongest variability on $\lesssim 1$ day time scales, with an RMS of 2.9% in the UVW2 filter; there were only 3 additional observations using either the UVW2 or U filter where the RMS was $> 1.8\%$. The current *XMM-Newton* data would thus seem to indicate that NGC 3227 is towards the top of the list of Seyferts which display strong UV continuum variability on $\lesssim 1$ day time scales. In NGC 3227, the X-rays are much more strongly variable on these time scales (RMS for the 0.2–1 and 3–10 keV light curves were 15.8% and 8.9%, respectively), a result similar to what Smith & Vaughan (2007) found for their sample.

Visually, it is tempting to connect the gradual brightening observed in the OM light curve with that observed simultaneously in the soft X-ray band during the *XMM-Newton* observation. However, the rise in soft X-ray flux ($\sim 40\%$) is much greater than that observed in the UV band ($\sim 10\%$). We calculated ICFs and Discrete Correlation Functions (DCF; Edelson & Krolik 1988) between the UV and soft X-ray light curves (the latter rebinned to 1400 s); the results are plotted in Figure 17, along with 90 and 95% confidence limits from the Bartlett method. We found no significant correlation: r_{max} peaks at only ~ 0.5 ; there are no “bends” or multiple trends in the OM light curve to drive a correlation. The warning regarding cross-correlation analysis performed on two unrelated red-noise light curves bear repeating: beware of spuriously high values of r_{max} (e.g., Welsh 1999) and treat values of r_{max} which are not very close to 1.0 with skepticism. The suggestion of a correlation between the soft X-ray band and the UV band, while visually tempting, is thus speculative at best.

9. DISCUSSION

We have analyzed a ~ 100 ks *XMM-Newton* long-look of NGC 3227, observed in December 2006. In both the EPIC-pn and RGS spectra, we have modeled the ionized X-ray absorber using two components, with very similar column densities, and with ionization parameters $\log \xi$ near 1.2 and 2.9 (in the RGS spectrum). With the RGS, we have constrained the outflow velocity of the high-ionization absorber to be $-(2060^{+240}_{-170}) \text{ km s}^{-1}$ relative to systemic. The best estimate for the outflow velocity relative to systemic for the low-ionization absorber is $-(420^{+430}_{-190}) \text{ km s}^{-1}$, though a wider range of possible outflow velocities cannot be ruled out at very high confidence. In §9.1, we discuss further details of these ionized outflows, including exploring connections to the low-velocity, very low ionization, dusty lukewarm absorber observed in the UV.

The steep soft excess, which does not seem to be affected by the same neutral material obscuring the hard X-ray

continuum, is shown with the EPIC pn to be rapidly variable compared to other Seyferts on $\lesssim 1$ day time scales; its normalization increases by $\sim 25\%$ in ~ 20 ks. The UV continuum light curve during the *XMM-Newton* observation also shows a relatively strong increase compared to most other Seyferts on $\lesssim 1$ day time scales. Possible origins for these behaviors are discussed in §9.2.

The hard X-ray power-law continuum in both the *XMM-Newton* pn and MOS fits and in the PCA + HEXTE + BAT fits is somewhat low, $\Gamma_{\text{HX}} \sim 1.5\text{--}1.6$. Using accumulated *RXTE* PCA and HEXTE archival data from over 6 years of monitoring, plus *Swift*-BAT 9-month survey data, we constrain the strength of the Compton reflection component R to be $\lesssim 0.5$. We also find the first evidence for a high-energy continuum cutoff in this source, at 90 ± 20 keV. The high-energy continuum is discussed further in §9.3.

The narrow Fe K α emission line at 6.4 keV is resolved in the pn spectrum. From time-resolved spectral fits to the *RXTE*-PCA data, we find tentative evidence for a significant fraction of the Fe K line flux to track variations in the continuum flux F_{2-10} on time scales of < 700 days. The 6.4 keV Fe K α line properties are discussed further in §9.4.

In addition, we find significant evidence for emission near 6.0 keV in both the pn and MOS 1+2 spectra. It is modeled approximately equally well as a narrow emission line or as the red wing to a relativistically-broadened Fe K emission line, as discussed in §9.5.

9.1. Overview of the X-ray absorbers

In the *XMM-Newton* RGS spectrum, we model two zones of absorption, with $\log \xi_{\text{lo}} = 1.21^{+0.18}_{-0.08}$ and $\log \xi_{\text{hi}} = 2.90^{+0.21}_{-0.26}$, and with very similar column densities, $N_{\text{H,lo}} = 1.1^{+0.1}_{-0.2} \times 10^{21} \text{ cm}^{-2}$ and $N_{\text{H,hi}} = 2.4^{+2.0}_{-1.2} \times 10^{21} \text{ cm}^{-2}$. Other AGN have been reported to host multiple warm absorber components with different ionization parameters but similar hydrogen column densities (see e.g., Blustin et al. 2005). The blueshift relative to systemic of the high-ionization absorber was significantly constrained, yielding an outflow velocity relative to systemic of $-(2060^{+240}_{-170}) \text{ km s}^{-1}$. The best-fit blueshift relative to systemic for the low-ionization absorber corresponded to an outflow velocity relative to systemic of $-(420^{+430}_{-190}) \text{ km s}^{-1}$; however, as this is primarily constrained by only two (possibly blended) absorption features, models with blueshifts ranging from zero to identical to that for the high-ionization absorber were not clearly rejected. It is therefore not clear if the two zones are physically and kinematically distinct or if there exists a single ionized absorber spanning a broad range of ionization levels, a possibility to consider if the ionized X-ray absorbing gas is spatially extended. For instance, Gonçalves et al. (2006) model the warm absorbing layers in NGC 3783 as a single constant-density gas component in pressure equilibrium.

To estimate the distance r between the central black hole and the outflowing gas in NGC 3227, we can use $\xi = L_{\text{ion}}/(nr^2)$, where n is the number density, and L_{ion} is the 1–1000 Ryd illuminating continuum luminosity. We estimate the maximum possible distance to the material by assuming that the thickness Δr must be less than the distance r_{max} . The column density $N_{\text{H}} = n\Delta r$, yielding

the upper limit $r_{\max} < L_{\text{ion}}/(N_{\text{H}}\xi)$. We estimate the unabsorbed 1–1000 Ryd flux to be $\sim 3 \times 10^{-10}$ erg cm $^{-2}$ s $^{-1}$, which corresponds to $L_{\text{ion}} \sim 1.5 \times 10^{43}$ erg s $^{-1}$ (using a distance of 20.3 Mpc, and assuming $H_0 = 70$ km s $^{-1}$ Mpc $^{-1}$ and $\Lambda_0 = 0.73$). Assuming two physically distinct warm absorbers, for the high-ionization X-ray absorber, this yields $r_{\max} = 3.6$ pc. For the low-ionization X-ray absorber, the constraints are even weaker: $r_{\max} = 150$ pc. These constraints are much poorer compared to that derived by Gondoin et al. (2003) for a one-zone absorber, $r_{\max} = 0.45$ pc, as those authors found a higher value for the column density and a lower value for the ionizing flux.

However, we can also derive a minimum radial distance from the black hole r_{\min} from the winds via the requirement for the outflow velocity v to be greater than the escape velocity: For the high-ionization X-ray absorber, $r_{\min} = (c^2/v^2)R_{\text{g}} = 17000R_{\text{g}} = 40$ light-days, placing it outside both the BLR and the inner radius of the dust as reverberation-mapped by Suganuma et al. (2006).

Under the assumption that the gas is in equilibrium and that the outflow velocity is a constant, the mass outflow rate \dot{M}_{out} of the X-ray absorbers can be derived via conservation of mass: $\dot{M}_{\text{out}} = \Omega n r^2 v m_{\text{p}}$, where v is the outflow velocity, m_{p} is the proton mass, and Ω is the covering fraction. We then substitute $n r^2 = L_{\text{ion}}/\xi$. Assuming $\Omega = 0.3$ (arbitrary), we find, for the high-ionization absorber, $\dot{M}_{\text{out}} \sim 2 \times 10^{24}$ gm s $^{-1} \sim 0.03 M_{\odot}$ yr $^{-1}$. For the low-ionization absorber, assuming $v = 420$ km s $^{-1}$, $\dot{M}_{\text{out}} \sim 2 \times 10^{25}$ gm s $^{-1} \sim 0.3 M_{\odot}$ yr $^{-1}$. We note that the actual outflow rate should be lower if there is an extreme degree of collimation along the line of sight. We can compare the outflow rate to the inflow accretion rate \dot{M}_{acc} using $L_{\text{bol}} = \eta \dot{M}_{\text{acc}} c^2$, where η is the accretion efficiency parameter, typically 0.1. Woo & Urry (2002) estimate L_{bol} for NGC 3227 to be 7.2×10^{43} erg s $^{-1}$, which means an accretion rate relative to Eddington, $L_{\text{bol}}/L_{\text{Edd}}$, of 1.4%. For $\eta = 0.1$, $\dot{M}_{\text{acc}} = 0.01 M_{\odot}$ yr $^{-1}$. The kinetic power associated with the outflow component, estimated as $\dot{M}_{\text{out}} v^2$, is thus in the approximate range 10^{40-41} erg s $^{-1}$.

The outflow mass rate and kinetic energy are rough estimates only, but it does appear likely that the outflows represent at least a large fraction of the AGN's accretion rate. If the X-ray ionized outflows are long-lived, then a sustained feeding of the black hole would be difficult.

9.1.1. Helium-like emission line diagnostics

It is not obvious whether the emission lines detected in the RGS spectrum are due to collisional ionization or photo-ionization. We do not detect a strong Fe XVII L 3d–2p 1P_1 line at 826 eV, an indicator of collisional ionization. However, RRC lines, indicators of photo-excitation, are not obvious, either.

We can attempt to use diagnostics associated with the helium-like O and N emission triplets. In a collisionally-(photo-) ionized plasma, the resonance (forbidden) line dominates. However, in NGC 3227, there is not significant dominance of one of these lines in either emission triplet. The presence of helium-like absorption lines may be a factor: the emission and absorption lines are not completely separated in energy given the modeled blueshift of the absorption lines, the RGS resolution and the signal/noise ratio of the RGS data. This fact also complicates

our use of the density indicator $R \equiv f/i$ and the temperature indicator $G \equiv (f + i)/r$ (e.g., Porquet & Dubau 2000) where f , i and r are the intensities of the forbidden, intercombination, and resonance lines, respectively (i is the summed intensity of both intercombination lines). As G depends on r , it can indicate whether photo-ionization dominates or whether a photo-/collisional-ionization hybrid is applicable (Porquet & Dubau 2000). Porter & Ferland (2007) warn that although G indicates temperature in a collisionally-ionized plasma, it should not be used as a temperature indicator in a photo-ionized plasma (in addition, see Porter & Ferland 2007 for warnings regarding usage of R as density indicator in photo-ionized plasmas).

For the O VII emission triplet in NGC 3227, we measure $G = 4.7^{+9.3}_{-4.0}$; $G < 2.0$ for the N VI triplet. Uncertainties here are statistical only and do not include systematic effects associated with the presence of absorption lines. These values thus do not yield any useful constraints on whether collisional- or photo-ionization dominates. For the O VII emission triplet, $R = 1.4^{+1.0}_{-0.9}$. Assuming the plasma is either purely ionized or a hybrid of collisionally- and photo-ionized material, and assuming a temperature near 10^6 K, electron densities of roughly $10^{10.5-11.5}$ cm $^{-3}$ are implied (Porquet & Dubau 2000). For either collisional or photo-ionization, densities above 10^{12} cm $^{-3}$ are ruled out by the presence of the strong O VII (f) line.

9.1.2. Long-term variability in the cold and ionized absorbers

Variations in the column density of neutral absorbing gas along the line of sight has been reported to occur on a wide range of time scales (days to years) in both Seyfert 1 AGN (e.g., I Zw 1, Gallo et al. 2007; NGC 4151, Puccetti et al. 2007; NGC 3516, Turner et al. 2008, Markowitz et al. 2008) and Seyfert 2 AGN (Risaliti et al. 2002, 2005). NGC 3227 is no exception, given the 2000-1 obscuring event by a lowly-ionized ($\log \xi \sim 0$) dense cloud of column density 2.6×10^{23} cm $^{-2}$ and inferred to be located in the BLR (Lamer et al. 2003). That cloud is likely physically distinct from the local cold gas and the ionized X-ray absorbers, as $N_{\text{H,local}}$, $N_{\text{H,WA1}}$ and $N_{\text{H,WA2}}$ modeled from the 2006 *XMM-Newton* observation are much lower than that for the 2000-1 obscuring cloud. Nonetheless, there does seem to be evidence for variations in $N_{\text{H,local}}$ on time scales of years in NGC 3227: George et al. (1998b) noted $N_{\text{H,local}}$ to increase from $\sim 3 \times 10^{20}$ cm $^{-2}$ in 1993 to $\sim 3 \times 10^{21}$ cm $^{-2}$ by 1995. Gondoin et al. (2003) reported $N_{\text{H,local}} = 7 \times 10^{20}$ cm $^{-2}$ from the 2000 *XMM-Newton* observation; that value is the same as the column here in the 2006 EPIC-pn spectrum. Assuming that discrepancies in values of $N_{\text{H,local}}$ inferred from different missions are intrinsic to the source and not due to cross-instrumental calibration uncertainties, the range in measured $N_{\text{H,local}}$ values would suggest the presence of cold gas along the line of sight at $<<$ pc radii from the black hole.

George et al. (1998b) noted an increase in the ionized absorber column density, from $\sim 3 \times 10^{21}$ cm $^{-2}$ in 1993 to $\sim 3 \times 10^{22}$ cm $^{-2}$ 1995, ruling out a location outside the NLR. The value of $N_{\text{H,WA}}$ obtained by Gondoin et al. (2003) using XSTAR modeling is $2.7 \pm 0.7 \times 10^{21}$ cm $^{-2}$. Variability in $N_{\text{H,WA}}$ between 2000 and 2006 is thus implied to be significant only at the 2.3σ confidence level. Further-

more, Gondoin et al. (2003) did not include a component to model a soft X-ray excess; if the soft excess was intrinsically present during the 2000 observation, then their estimate of $N_{\text{H,WA}}$ would be too high. Assuming the variations in $N_{\text{H,WA}}$ since 1993 to be real, then at least some fraction of the ionized X-ray absorbing gas is likely present at $<< \text{pc}$ radii.

9.1.3. Possible connections between the X-ray and UV ionized absorbers

The extended dusty lukewarm absorber (hereafter DLWA) studied by Crenshaw et al. (2001) may be a physically and/or kinematically distinct component from the ionized X-ray absorbers. Crenshaw et al. (2001) report the ionization parameter U of the DLWA to be 0.13 (see George et al. 1998a for definitions of the optical/UV ionization parameter U and the X-ray ionization parameter U_{x}). Assuming an optical-to-X-ray spectral index α_{ox} (estimated from photometric measurements taken from NED), and using the conversions from Figure 1 of George et al. (1998a), $U/U_{\text{x}} \sim 250$ and $\xi/U_{\text{x}} \sim 5000$, we can translate our best-fit ionization parameters for the low- and high-ionization X-ray absorbers, $\log \xi = 1.21$ and $\log \xi = 2.90$, respectively, into corresponding values of $U = 1.0$ and 40 . The values of the ionization parameters for the DLWA and the low-ionization X-ray absorber are not too dissimilar, tentatively suggesting a possible physical connection. However, it is not possible to definitively link the DLWA and the low-ionization X-ray absorber in velocity space, as, other than the Fe UTA and O VII edge, there are no strong X-ray absorption features >0.35 keV endemic to only the low-ionization, and not the high-ionization, X-ray absorber at the best-fit ionization parameter values.

Crenshaw et al. (2001) note that the column density of the DLWA is $2 \times 10^{21} \text{ cm}^{-2}$, very similar to that measured for both X-ray absorbers here. The outflow velocities relative to systemic of DLWA lines (tens of km s^{-1}) are much lower than that of at least the high-ionization X-ray absorber ($\sim 1500 - 2000 \text{ km s}^{-1}$). Furthermore, it is likely that the DLWA has a high covering fraction (Crenshaw et al. 2001). We cannot rule out the possibility that the low-ionization X-ray absorber may be the inner edge of the extended DLWA. Moreover, it is conceivable that the outflowing, ionized X-ray absorbers may supply the extended, 100-pc scale DLWA gas (at least along the line of sight), with the velocity slowing and ionization parameter decreasing as the distance from the black hole increases. If the X-ray ionized absorbing gas is continuously feeding the UV absorber, we might expect the existence of an “intermediate” zone of absorbing material with outflow velocity between those of the observed X-ray and UV ionized absorbers. Confirmation of such a zone would strengthen the physical connection between the X-ray and UV ionized absorbers. However, clarification of whether or not the X-ray absorbing outflow is sustained or intermittent would be needed to determine the exact physical and kinematic connection between the UV and X-ray absorbers.

The properties we have derived for the ionized X-ray absorbers are consistent with the notion that dust may be swept up by an outflowing wind at radii \gtrsim a few light-days (outside the BLR, where dust cannot survive). However, the current data cannot distinguish between a dusty and

a dust-free X-ray ionized absorber; as discussed in §5, the upper limit on the neutral Fe L3 dust edge in the RGS spectrum corresponds to a hydrogen column density consistent with that implied by optical line absorption.

9.2. The variable soft excess in NGC 3227

The origin of the soft excess emission in NGC 3227 is not immediately obvious. The soft excess does not undergo the same obscuration by cold material as that suffered by the hard X-ray continuum. However, the large discrepancy between Γ_{SX} and Γ_{HX} argues against both partial covering scenarios and against the soft X-rays being nuclear power-law emission scattered in an extended region. We have modeled the soft excess in NGC 3227 using a blackbody component to represent direct thermal emission from accretion disk, but such a model seems to be unphysical given the apparent consistency of blackbody parameters across a wide range of Seyfert properties, including black hole mass (e.g., Gierliński & Done 2004). We have also modeled the soft excess as inverse Comptonization of seed photons, likely thermal optical and UV photons from the accretion disk, by thermal electrons (Sunyaev & Titarchuk 1980). Such a mechanism could conceivably operate in the hot, ionized surface of the accretion disk (Hubeny et al. 2001; Janiuk, Czerny & Madejski 2001).

In Seyferts, soft excesses have been seen to vary on time scales of weeks, e.g., as seen in the narrow line Seyfert 1s Ark 564 and Ton S180 (Edelson et al. 2002). The soft excess in the quasar 3C 273 has also been known to vary on time scales of \sim a week (Kim 2001 and references therein). Vaughan et al. (2002) found the soft excess of the NLSy1 Ton S180 to vary rapidly, though in concert with the hard X-ray power law component, leading to measurements of F_{var} roughly independent of energy band across the EPIC bandpass. However, most other Seyferts’ F_{var} spectra peak near 1–2 keV (e.g., Arévalo et al. 2008; Vaughan & Fabian 2004). This is commonly explained with a variable power-law component superimposed over a constant or relatively less variable hard component above ~ 5 keV (likely the Compton reflection hump) and a constant or less variable soft component below ~ 1 keV (the soft excess). In NGC 3227, however, F_{var} increases with decreasing energy below 1 keV (Figure 14) due to a soft excess that is strongly variable in normalization.

The simultaneous increases in UV and soft X-ray continuum flux are not statistically significantly correlated, so a direct UV–soft X-ray connection is tenuous at best. However, if such a connection were real, and if both the UV and soft X-ray originate in the same location on the disk, a rapid change in illumination of the accretion disk could explain the simultaneous increases.

We can investigate if the observed UV trend can be attributed to thermal reprocessing of the increasing soft X-ray flux trend by the accretion disk. Given the black hole mass, accretion rate, and assuming a standard thin disk with an inner radius of $6 R_{\text{g}}$, 90% (50%, 10%) of the 260 nm continuum emission originates from within 60 (25, 10) R_{g} . The light crossing time across the diameter of the disk at a $60 R_{\text{g}}$ radius is roughly 20 ks. In a thermal reprocessing scenario, the UV flux should track the soft X-ray flux and be smeared on a time scale < 20 ks, assuming that the soft X-ray continuum emitting region is located near

the central disk plane. If the soft X-ray emitting region is located well off the plane, the light travel time to the UV-emitting part of the disk is increased (e.g., 30 ks travel time for a height of $100 R_g$.) The light curves displayed in Figure 1 are consistent with this scenario, as any soft X-ray to UV lag is less than several tens of ks.

Another possibility is that the soft X-ray continuum flux originates in inverse Comptonization of UV seed photons from the disk; e.g., the scenario associated with the COMPST model. However, the fact that the observed increase in the soft X-ray flux (40%) is stronger than the observed increase in the UV flux (10%) would argue against all of the soft X-ray photons being passively-reprocessed UV photons, unless only the soft X-ray photons were anisotropically beamed along the line of sight, or unless the soft X-ray flux is responding to a comparative increase in the UV continuum flux that occurred less than a few tens of ks before the start of the *XMM-Newton* observation.

In the inverse Comptonization scenario, and in the absence of thermal reprocessing, the UV variability would have to be intrinsic to the disk. We can consider inwardly-propagating variations in the local mass accretion rate (e.g., Lyubarski 1997, Arévalo & Uttley 2006), specifically, the case where the fluctuations travel on the viscous time scale. To produce the 10% observed variation, such a propagating fluctuation would have to modify 20% of the flux contained within a radius of $25 R_g$, or 100% of the flux contained within a radius of $10 R_g$. Let us consider the former case: a fluctuation that propagates with an inward velocity that takes it from a radius of $25 R_g$ to the innermost stable disk radius of $6 R_g$ over 100 ks, while modulating 20% of the flux within $25 R_g$, could produce the observed UV variability. However, the required velocity, $\sim 1/5$ of the orbital velocity, is very high for a standard disk (Shakura & Sunyaev 1973): to be the viscous velocity for a standard disk, one would need $(H/R)^2 \alpha = 0.2$ (H , R , and α are the height, radius and viscosity parameters, respectively), i.e., a very thick disk with a large viscosity parameter, which is probably not adequate for the optical-emitting portion of the disk. The UV variability is thus likely not associated with accretion rate fluctuations traveling on viscous time scales. The sound speed near $25 R_g$ (assuming $\alpha = 0.1$) is roughly two orders of magnitude slower than the orbital speed, and sound waves are thus likely inadequate to produce the required flux modification in 100 ks.

The rapidly variable soft excess is qualitatively similar to that observed in 3C 120 with *Suzaku* by Kataoka et al. (2006), who model the variable soft excess in that object as the high-energy part of a synchrotron jet component. The rapid variability observed in the soft X-ray and UV bands in NGC 3227, and the fact that the soft excess undergoes less absorption by cold material compared to the hard X-ray continuum, may also be consistent with existence of such a jet component, in addition to and independent of the accretion disk corona (hard X-ray) emission. Unlike 3C 120, NGC 3227 is of course a radio-quiet AGN. A ~ 40 pc scale jet was detected in NGC 3227 by the VLA in a 1991 observation (Kukula et al. 1995), though 10-100 pc scale jets are common in Seyferts (e.g., Gallimore et al. 2006). Broad band spectral energy distribution (SED) modeling of an accretion disk + jet is beyond the scope of this paper; constraining such an SED component would

be complicated by the presence of absorbing dust in the poorly-studied EUV band. However, such a component is plausible if its peak in νL_ν space were near 10^{14-16} Hz (explained if the jet were young, e.g., 10^{4-5} yrs), and the total observed synchrotron power were no more than 10^{41-42} erg s $^{-1}$. In this scenario, the observed UV continuum emission would be a mixture of slowly-varying "big blue bump" emission from the accretion disk plus rapidly variable synchrotron emission (which would contribute less than $\sim 50\%$ to the total observed UV continuum flux).

9.3. The high energy emission components

The photon index of the power-law component used to model the hard X-ray continuum emission in both the *XMM-Newton* and *RXTE* data is rather low ($\Gamma_{\text{HX}} \sim 1.5 - 1.6$) compared to traditional or "canonical" values of $\sim 1.8 - 1.9$ for most broad-line Seyfert 1 AGN. However, similarly low values of Γ_{HX} have been reported previously for this object (e.g., George et al. 1998b). The presence of a cutoff near 100 keV, as implied by both the *Swift*-BAT and the *RXTE*-HEXTE data, would suggest thermal Comptonization, but better data in the 50–200 keV band and above are needed to confirm the cutoff and better constrain its energy. The low-energy rollover to the hard X-ray continuum component was modeled above as being due to cold absorption, but could also potentially be a signature of Comptonization, as it is possible for Comptonized continua to have a low-energy rollover e.g., below 1 keV depending on parameters such as the distribution of input photon field (e.g., Titarchuk 1994).

The 7.1 keV edge is likely due to reflection, as the absorbing components modeled here predict an edge depth much too small to detect here. However, the strength of the Compton reflection component R is measured to be low ($\lesssim 0.5$), suggesting that Compton-thick material exists in only a small fraction of the sky as seen from the continuum source. For example, the putative Compton-thick molecular torus invoked in standard Seyfert 1/2 unification schemes (Urry & Padovani 1995) could be weak or small. Another possibility is that the optically-thick accretion disk could be truncated, or the inner accretion disk could transition into an optically-thin, radiatively inefficient flow, e.g., an ADAF or RIAF (Narayan & Yi 1994, 1995; Blandford & Begelman 1999; Narayan et al. 2000). Such flows are frequently invoked when describing low accretion rate accreting black hole systems (e.g., low luminosity AGN). In addition, Liu et al. (2007) forward a model for low accretion rate flows in which optically-thin coronal matter condenses into a cool, optically-thick inner disk, for $L_{\text{Bol}}/L_{\text{Edd}} = 0.1 - 2\%$ (assuming values for the viscosity parameter $\alpha \sim 0.1 - 0.4$). Condensation radii of a few tens of R_g are plausible.

Wu & Gu (2008) noted that for both black hole X-ray binary systems and AGN accreting above a critical "transition" value of $L_{\text{Bol}}/L_{\text{Edd}}$, Γ_{HX} correlates with $L_{\text{Bol}}/L_{\text{Edd}}$. Below this transition, Γ_{HX} and $L_{\text{Bol}}/L_{\text{Edd}}$ anti-correlate. Wu & Gu (2008) suggest that the transition between a thin disk and an ADAF-type flow occurs near $L_{\text{Bol}}/L_{\text{Edd}} = 1\%$ for black hole X-ray binary systems and near 0.3% for AGN. The corresponding value of Γ_{HX} at this transition point is 1.5, similar to that observed in NGC 3227 ($L_{\text{Bol}}/L_{\text{Edd}} = 1\%$). This suggests that the accretion flow

in NGC 3227 may be consistent with either a thin disk, a ADAF-type flow, or a transition to both.

9.4. The Narrow Fe K α line at 6.4 keV

The measured energy of the Fe K α emission line is consistent with an origin in neutral material. The line is resolved in the pn spectrum; the measured width σ of 65 ± 14 eV translates into a FWHM velocity v_{FWHM} of 7000 ± 1500 km s $^{-1}$. This velocity width is similar to that for the H β line, 5500 ± 500 km s $^{-1}$ (Wandel et al. 1999), suggesting an origin for the Fe K line in material commensurate with the BLR.

Assuming Keplerian motion, and assuming the velocity dispersion is related to the FWHM velocity as $\langle v^2 \rangle = \frac{3}{4} v_{\text{FWHM}}^2$ (Netzer et al. 1990), assuming a black hole mass M_{BH} of $4.22 \pm 2.14 \times 10^7 M_{\odot}$ (Peterson et al. 2004), we can use $GM_{\text{BH}} = r \langle v^2 \rangle$ to estimate the radius r of the line-emitting material. We find $r = 7.2^{+12.7}_{-4.9}$ light-days, equivalent to $3000^{+5300}_{-2100} R_g$. This value is consistent with the radius of < 700 light-days inferred from the very crude reverberation mapping discussed in §6.2. It is also consistent with the BLR (H β) region radius of 9^{+6}_{-8} light-days (Peterson et al. 2004), as well as with the ~ 5 –20 light-day inner radius of the dust as reverberation-mapped by Suganuma et al. (2006).

The Fe line-emitting material may be spatially extended in NGC 3227; only the innermost regions have had time to respond to continuum variations, which may get smoothed out by the outer regions anyway. Alternatively, we note in Figure 16 that extrapolation of the $F_{2-10} - I_{\text{FeK}\alpha}$ relation to zero continuum flux results in a non-zero offset. That is, there may exist Fe-line emitting material which does not respond to the continuum flux, and only some fraction of the total observed Fe line flux responds to the continuum variations on < 700 light-days. Either of these two ideas may explain why F_{var} for the 2–10 keV continuum flux is larger than that for the Fe line.

The observed line EW is 91 ± 10 eV. The column density of the gas required to produce such an emission line must be greater than 10^{22} cm $^{-2}$, otherwise the optical depth would be insufficient to produce such a prominent line. However, the lack of an obvious Compton shoulder (the emission near 6.0 keV was not identified as such) would argue against the bulk of the line photons originating in Compton-thick material.

Let us first assume an origin in optically-thin gas that completely surrounds a single, isotropically-emitting continuum source (covering fraction $f_c = 1$) and is uniform in column density. We can relate EW to N_{H} using the following equation, taken from e.g., Markowitz et al. (2007):

$$EW_{\text{calc}} = f_c \omega f_{K\alpha} A \frac{\int_{E_{\text{Kedge}}}^{\infty} P(E) \sigma_{\text{ph}}(E) N_{\text{H}} dE}{P(E_{\text{line}})} \quad (1)$$

ω is the fluorescent yield: the value for Fe, 0.34, was taken from Kallman et al. (2004). $f_{K\alpha}$ is the fraction of photons that go into the K α line as opposed to the K β line; this is 0.89 for Fe I. A is the number abundance relative to hydrogen; solar abundances, using Lodders (2003), were used. $P(E)$ is the spectrum of the illuminating continuum at energy E ; E_{line} is the K α emission line energy.

$\sigma_{\text{ph}}(E)$ is the photo-ionization cross section assuming absorption by K-shell electrons only; all cross sections were taken from Veigele (1973¹⁹). The observed Fe K α EW can thus be produced from material with $N_{\text{H}} = 1.4 \pm 0.2 \times 10^{23}$ cm $^{-2}$. Similarly, the observed Ni K α line EW of 13^{+13}_{-10} eV indicates $N_{\text{H}} = 3.9^{+3.9}_{-2.9} \times 10^{23}$ cm $^{-2}$.

If the absorbers are instead clumpy and lie out of the line of sight, we can use Eqn. 1 of Wozniak et al. (1998), which gives the expected Fe K α line intensity for a cloud with a column $\gtrsim 10^{23}$ cm $^{-2}$ lying off the line of sight and subtending a fraction $\Omega/4\pi$ of the sky as seen from a single, isotropically-emitting continuum source. Assuming solar abundances and given the observed Fe K α line intensity, for values of $\Omega/4\pi = 0.1$ (0.3), a column density of 1.5×10^{23} (5×10^{22}) cm $^{-2}$.

In either case, the derived column density is higher than that of the hard X-ray absorbing material in the SXPL and COMPST model fits to the *XMM-Newton* EPIC data. It is, however, closer to the column density of the obscuring cloud during the 2000-1 obscuring event (Lamer et al. 2003). Based on the duration of the obscuring event and the implied number density, that cloud was inferred to be located in the BLR. The similarities in column density and inferred location suggest a connection between the Fe line-emitting material and the obscuring cloud of 2000-1.

9.5. Emission at 6.0 keV

The Fe K emission profiles in both the pn and MOS 1+2 spectra suggest emission redward of the Fe K α core. However, the present data cannot distinguish between a model wherein the emission near 6.0 keV is due to a narrow emission line or is instead the red wing of a relativistically broadened Fe K α line with an EW near 80 eV.

9.5.1. A narrow emission feature?

We first discuss the emission in the context of modeling it as a narrow feature. In the pn spectrum, the line width σ was < 200 eV; the EW was 21^{+19}_{-9} eV. High-resolution spectroscopy has yielded evidence for similar narrow emission features in roughly 16 Seyferts to date (see Vaughan & Uttley 2008 for a review). These features are commonly interpreted as red- or blue-shifted Fe K features associated with "hot-spots," localized areas of the accretion disk illuminated by a localized flare just above the disc (possibly due to magnetic reconnection), rather than a central illuminator or an extended corona (e.g., Dovčiak et al. 2004, Goosmann et al. 2007).

Vaughan & Uttley (2008) point out that these narrow emission features are rarely reported at more than 3.0σ confidence. Consideration of selection bias and publication bias brings skepticism to the validity of these features and raises the possibility that a non-trivial fraction of these published lines may be consistent with being due to photon noise. In the case of the pn spectrum of NGC 3227, the Monte Carlo simulations we performed suggested that the line was detected at $> 99.9\%$ confidence (i.e., $< 0.1\%$ likelihood that it is due to photon noise). However, we caution that the Monte Carlo procedure yields an estimate of the detection significance independently of the existence of other high-resolution spectra of NGC 3227 and other Seyferts. On the other hand, the marginal detection of the

¹⁹ <http://www.pa.uky.edu/~verner/photo.html>

emission feature near 6.1 keV in the MOS 1+2 spectrum, simultaneously to the pn data, reduces the likelihood that the feature is due to photon noise. In addition, the value of $|\Delta\chi^2|$ associated with modeling the line in the pn spectrum is among the largest reported for narrow emission lines (See Table 1 of Vaughan & Uttley 2008).

If the feature near 6.0 keV is indeed emission from a "hot spot" on the accretion disk, we can estimate its radial distance from the black hole. For instance, we can assume that the observed redshifting is due solely to Doppler shifting associated with Keplerian motion of the receding side of the disk. We use the 3σ energy range of 5.8 to 6.3 keV, corresponding to radial velocities along the line of sight v_r of $0.02\text{--}0.09c$ (assuming an origin in neutral Fe). Assuming the disk is inclined by $i = 30^\circ$ (45°) with respect to the plane of the sky, using $M_{\text{BH}} = 4.2 \times 10^7 M_\odot$ (Peterson et al. 2004), and ignoring gravitational redshifting, this corresponds to Keplerian motion at radii of roughly 12–430 (25–800) R_{Sch} .

If the flare is co-rotating with the disk, then a minimum radius independent of i is defined by the fact that the line energy is consistent with being constant and redward of 6.4 keV for the 100 ks duration of the observation. Any orbital period < 100 ks is excluded; otherwise the number of photons > 6.4 keV would be greater than the number of photons < 6.4 keV. Radii $< 9 R_{\text{Sch}}$ are thus excluded.

An alternate possibility is that the line-emitting material is in free-fall, with no velocity component transverse to our line of sight. Yet another possibility is that the observed redshifting is purely due to energy losses of photons escaping from the vicinity of the black hole; assuming for simplicity emission from neutral Fe originating in gas lying along the line of sight to the black hole, with all velocity transverse to line of sight, radii of $\sim 6 - 30 R_{\text{Sch}}$ are plausible.

Another speculative possibility is that the line-emitting material could be associated with the base of the jet, forming above the accretion disk, as opposed to being a part of the accretion disk. Close to the rotation axis in AGN, magnetic fields are likely twisted by the differential rotation of the disk, serving to launch and collimate jets (e.g., Blandford & Payne 1982). For instance, Marscher et al. (2008) presented observational evidence for the jet in the radio-loud AGN BL Lac to follow a spiral flow as it is accelerated through a zone containing a helical magnetic field. The 6.0 keV line in NGC 3227 may be emission from Fe in a blob of material, with a column density N_{H} of $10^{21\text{--}22} \text{ cm}^{-2}$, which has been caught up in the launching and formation of the weak jet. If the material is close to the axis, above the disk, and moving with a velocity with a large azimuthal component, then an observed redshift is possible unless the rotation axis lies very close to the line of sight. However, the weakness of Seyferts' jets may possibly be attributed to weaker acceleration and/or collimation mechanisms compared to those in blazars, reducing the likelihood that such azimuthal velocities can exist in Seyferts.

9.5.2. A relativistically broadened diskline component?

Evidence for relativistically broadened Fe line "diskline" profiles in a significant fraction of Seyferts has been accumulating since the days of *ASCA* (Tanaka et al. 1995, Fabian et al. 2000). In recent years, *XMM-Newton* and *Chandra*-HETGS observations have demonstrated that a narrow core at 6.4 keV is ubiquitous; accurately modeling that component, as well as absorption due to ionized gas in the line of sight, is critical for accurate measurement of the flux and profile of any broad Fe line present.

In NGC 3227, our best-fit "DL" model incorporates a narrow Fe $K\alpha$ core, and suggests a relatively weak broad line, with an EW of 81^{+42}_{-30} eV. We constrained the inner radius to be $< 22 R_g$ and the inclination to be $< 25^\circ$ (though these values were derived with the radial emissivity parameter fixed at -3).

Assuming solar abundances, the abundances of Lodders (2003), and given the measured strength of the Compton reflection component $R = 0.40 \pm 0.07$, the predicted Fe line EW (George & Fabian 1991)²⁰ is 54 ± 9 eV, consistent with the modeled EW of the observed broad Fe line. The low value of the broad line EW may also suggest that the optically-thick disk is not spatially extended, again consistent with the notion that the nucleus of NGC 3227 could harbor an ADAF or RIAF, and the upper limit on the inner radius of $22 R_g$ is potentially consistent with the model of Liu et al. (2007) containing a small, optically-thin disk.

10. CONCLUSIONS

We have observed the nucleus of the Seyfert 1.5 AGN NGC 3227 with *XMM-Newton* in December 2006 for almost 100 ks. We have used EPIC and RGS spectra to study the Fe K bandpass, ionized absorbers, and 0.2–10 keV continuum in detail. We also present X-ray continuum light curves and a UV continuum light curve obtained with the Optical Monitor. We have combined these data with archival *RXTE*-PCA and *HEXTE* monitoring, plus *Swift*-BAT monitoring data, to constrain the level Compton reflection, study the high energy continuum up to 200 keV, and track the flux behavior of the Fe K line on time scales of weeks to years. Our main results are summarized as follows:

The EPIC pn spectrum shows the prominent narrow Fe $K\alpha$ emission line to be consistent with an origin in neutral Fe (Gaussian energy centroid 6.403 ± 0.009 keV). Its intensity and EW are $3.5 \pm 0.4 \times 10^{-5} \text{ ph cm}^{-2} \text{ s}^{-1}$ and 91 ± 10 eV, respectively, consistent with an origin in material with a column density $10^{22.5\text{--}23} \text{ cm}^{-2}$. The line is resolved in the pn spectrum, with a FWHM velocity $7000 \pm 1500 \text{ km s}^{-1}$. Assuming purely Keplerian motion, we estimate the radius of the line-emitting material to be $7.2^{+12.7}_{-4.9}$ light-days. The FWHM velocity and estimated radius are consistent with the BLR (as mapped by $H\beta$ emission) as well as with the $\sim 5\text{--}20$ light-day inner radius of the dust as reverberation-mapped by Suganuma et al. (2006).

Time-resolved spectral fitting to the 1999–2005 *RXTE*-PCA monitoring data reveal tentative evidence for a significant fraction of the Fe K line photons to track variations seen in the continuum, with a light travel time delay which is not tightly constrained, but is < 700 days. We thus rule

²⁰ George & Fabian 1991 predict $R = EW/150$ eV, using the abundances of Morrison & McCammon (1983), which assumed 3.3×10^{-5} Fe atoms per H atom. Lodders (2003) sets the Fe abundance to 2.95×10^{-5} Fe atoms per H atom.

out the possibility that the bulk of the (variable) Fe line photons originate at distances of 1–2 pc and more, e.g., in a multi-pc-scale molecular torus. However, more intensive sampling on time scales of days to weeks is required to better constrain the lower limit on the continuum–line lag.

Emission near 6.0 keV is detected in both the pn and MOS 1+2 spectra. The fact that it is detected in both instruments and the relatively large associated value of $\Delta\chi^2$ both argue against this feature being an artifact due to photon noise. It is inconsistent with being a Compton shoulder to the 6.4 keV Fe K α line. We modeled the emission using a narrow Gaussian component, with energy centroid (in the pn spectrum) $6.04^{+0.18}_{-0.04}$ keV, width $\sigma < 200$ eV, intensity $9^{+8}_{-4} \times 10^{-6}$ ph cm $^{-2}$ s $^{-1}$ and EW of 21^{+19}_{-9} eV. A possible origin is a “hot-spot” in the accretion disk, originating at radii of tens to hundreds of R_g . The emission feature is modeled equally well as the red wing to a relativistically broadened “diskline” component, with inner radius $< 22 R_g$, inclination $< 25^\circ$, and $EW = 81^{+42}_{-30}$ eV.

Broadband (0.2–10 keV) EPIC spectral modeling reveals a strong soft excess dominating below 1 keV. In the pn spectrum, the soft excess is fit well by a steep power law, with $\Gamma_{\text{SX}} \gtrsim 3$. A blackbody component and a low-temperature Comptonization component each fit the data well, though the physical plausibility these latter two components in Seyferts is not generally accepted. The normalization of the soft excess increases by about 20% during the first ~ 20 ks of the *XMM-Newton* observation, and by $\sim 40\%$ over ~ 50 ks. The soft X-ray band is more strongly variable than the hard X-ray band on time scales of tens of ks: unlike the F_{var} spectra of many other Seyferts, the F_{var} spectrum of NGC 3227 below 1–2 keV continues to increase as photon energy decreases. Such relatively rapid variability in the soft excess, independent of rapid variability in the hard X-ray band is very rare for Seyferts.

The OM shows the UV continuum flux (near 260 nm) to increase by 10% during the *XMM-Newton* observation. Such $\lesssim 1$ day variability is relatively strong compared to similar-duration UV continuum light curves obtained with the OM (Smith & Vaughan 2007).

We present the highest-quality gratings spectrum obtained for NGC 3227 to date. In the RGS spectrum, we model the ionized absorption using two zones. The higher-ionization zone has $\log \xi_{\text{hi}} = 2.90^{+0.21}_{-0.26}$, and an outflow velocity relative to systemic of $-(2060^{+240}_{-170})$ km s $^{-1}$. This indicates a minimum radial distance from the black hole of 40 light-days, placing it outside the BLR radius. The lower-ionization zone has $\log \xi_{\text{lo}} = 1.21^{+0.18}_{-0.08}$ (corresponding to a factor of roughly 3–10 higher than the dusty lukewarm

absorber modeled by Kraemer et al. 2000 and Crenshaw et al. 2001). Its main signature is a Fe M shell UTA near 740–780 eV. The best estimate for its outflow velocity relative to systemic is $-(420^{+430}_{-190})$ km s $^{-1}$. We find no evidence for non-solar abundances. Both absorbing zones have column densities $N_{\text{H,WA}}$ near $1 - 2 \times 10^{21}$ cm $^{-2}$. $N_{\text{H,WA}}$ and the column densities of local, cold absorption measured from the EPIC spectra are too low to be directly associated with the obscuring BLR cloud in 2000–1 studied by Lamer et al. (2003). However $N_{\text{H,WA}}$ is similar to that of the 100-pc scale DLWA, consistent with the notion that the outflowing X-ray absorbing material may supply the UV-absorbing DLWA material.

In the RGS spectrum, we detect five narrow emission lines detected at the systemic redshift; we identify these lines as being due to N VI (r), N VII, and the (f), (i) and (r) lines of O VIII. No emission due to Fe XVII L line (3d–2p) at 826 eV (a signature of collisionally-ionized plasma) is detected (upper limit of 1 eV). No strong RRC features due to H- or He-like ions (signatures of photo-ionized plasma) are detected (upper limits range from 5 to 50 eV).

We presented the total spectrum derived from *RXTE*-PCA and HEXTE archival monitoring data taken in 1996 and from 1999–2005, and combined them with a 4-channel Swift-BAT spectrum from the 9-month survey data (obtained in 2005). The HEXTE and BAT spectral data reported here represent the first detailed spectrum of NGC 3227 above ~ 20 keV and up to almost 200 keV. The hard X-ray continuum photon index in both the *RXTE*+BAT spectra and *XMM-Newton* EPIC spectra is rather flat, $\Gamma_{\text{HX}} = 1.5 - 1.6$. The strength of the Compton reflection hump is rather low, $R \lesssim 0.5$, consistent with the EW of the diskline component modeled in the pn spectrum (assuming solar abundances). We also find evidence for a high-energy continuum cutoff at 90 ± 20 keV.

The low values of Γ_{HX} and R , combined with the low value of $L_{\text{Bol}}/L_{\text{Edd}} \sim 1\%$, are consistent with the notion that NGC 3227 may harbor an optically-thin, radiatively-inefficient flow such as an ADAF, in addition to or instead of a standard geometrically-thin, radiatively-efficient disk.

A.M. thanks M. Elvis, A. Marscher and D. Evans for helpful suggestions. This work is based on an observation obtained with *XMM-Newton*, an ESA science mission, and has made use of HEASARC online services, supported by NASA/GSFC, the NASA/IPAC Extragalactic Database, operated by JPL/California Institute of Technology under contract with NASA, and the NIST Atomic Spectra Database.

REFERENCES

- Arévalo, P., McHardy, I.M., Markowitz, A., Papadakis, I.E., Turner, T.J., Miller, L. & Reeves, J.N. 2008, MNRAS, 387, 279
 Arévalo, P. & Uttley, P. 2006, MNRAS, 367, 801
 Arnaud, K. 1996, in *Astronomical Data Analysis Software and Systems*, Jacoby, G., Barnes, J., eds., ASP Conf. Series Vol. 101, p. 17
 Bearden, J.A. & Burr, A.F. 1967, Rev. Mod. Phys., 39, 125
 Bechtold, J., Czerny, B., Elvis, M., Fabbiano, G. & Green, R.F., 1987, ApJ, 314, 699
 Blandford, R. & Begelman, M.C. 1999, MNRAS, 303, L1
 Blandford, R.D. & Payne, D.G. 1982, MNRAS, 199, 883
 Blustin, A.J., Page, M.J., Fuerst, S.V., Branduardi-Raymont, G. & Ashton, C.E. 2005, A&A, 431, 111
 Brandt, W.N., Fabian, A.C., & Pounds, K.A. 1996, MNRAS, 278, 326
 Braito, V., Reeves, J.N., Dewangen, G.C. et al. 2007, ApJ, 670, 978
 Cohen, R.D. 1983, ApJ, 273, 489
 Courvoisier, T.J. & Paltani, S. 1992, IUE-Uniform Low Dispersion Archive Access Guide No. 4 (ESA-SP 1153A/B) (Noordwijk: ESA)
 Crenshaw, D.M., Kraemer, S.B., Bruhweiler, F.C., Ruiz, J.R. 2001, ApJ, 555, 633
 Crenshaw, D.M. & Kraemer, S.B. 2001, ApJ, 562, L29

- Crocombette, J.P., Pollak, M., Jollet, F., Thromat, N., & Gautier-Soyer, M. 1995, *Phys. Rev. B*, 52, 3143
- Crummy, J., Fabian, A.C., Gallo, L.C. & Ross, R.R. 2006, *MNRAS*, 365, 1067
- de Vaucouleurs, G., de Vaucouleurs, A., Corwin, H.G., Jr., Buta, R.J., Paturel, G. & Fouqué, P. 1991, *Third Reference Catalogue of Bright Galaxies* (New York: Springer)
- Dickey, J. & Lockman, F. 1990, *ARAA*, 28, 215
- Dovčiak, M., Bianchi, S., Guainazzi, M., Karas, V. & Matt, G. 2004, *MNRAS*, 350, 745
- Edelson, R. & Krolik, J.H. 1988, *ApJ*, 333, 646
- Edelson, R., Turner, T.J., Pounds, K.A., Vaughan, S.A., Markowitz, A., Marshall, H., Dobbie, P. & Warwick, R. 2002, *ApJ*, 568, 610
- Elvis, M. et al. 1994, *ApJS*, 95, 1
- Fabian, A.C., Iwasawa, K., Reynolds, C.S. & Young, A.J. 2000, *PASP*, 112, 1145
- Gallimore, J., et al. 2006, *AJ*, 132, 546
- Gallo, L.C., Brandt, W.N., Costantini, E., Fabian, A.C., Iwasawa, K. & Papadakis, I.E. 2007, *MNRAS*, 377, 391
- Gaskell, M.C. & Peterson, B.M. 1987, *ApJS*, 65, 1
- George, I.M. & Fabian, A.C. 1991, *MNRAS*, 249, 352
- George, I.M., Turner, T.J., Netzer, H., Nandra, K., Mushotzky, R.F., & Yaqoob, T. 1998a, *ApJS*, 114, 73
- George, I.M., Mushotzky, R.F., Turner, T.J., Yaqoob, T., Ptak, A., Nandra, K., & Netzer, H. 1998b, *ApJ*, 509, 146
- George, I.M., Mushotzky, R.F., Yaqoob, T., Turner, T.J., Kraemer, S., Ptak, A. & Nandra, K. 2001, *ApJ*, 559, 167
- Gierliński, M., Done, C. 2004, *MNRAS*, 349, L7
- Gierliński, M., Done, C. 2006, *MNRAS*, 371, L16
- Gonçalves, A.C., Collin, S., Dumont, A.-M., Mouchet, M. Różanska, A., Chevallier, L., & Goosmann, R.W. 2006, *A&A*, 451, L23
- Gondoin, P., Orr, A., Lumb, D. & Siddiqui, H. 2003, *A&A*, 397, 883
- Gonzalez Delgado, R.M. & Perez, E. 1997, *MNRAS*, 284, 931
- Goosmann, R.W., Mouchet, M., Czerny, B., Dovčiak, M., Karas, V., Różańska, A. & Dumont, A.-M. 2007, *A&A*, 475, 155
- Gu, M., Holczer, T., Behar, E. & Kahn, S.M. 2006, *ApJ*, 641, 1227
- Hubeny, I., Blaes, O., Krolik, J. & Agol, E. 2001, *ApJ*, 559, 680
- Janiuk, A., Czerny, B. & Madejski, G. 2001, *ApJ*, 557, 408
- Kallman, T.R., Palmeri, P., Bautista, M.A., Mendoza, C., Krolik, J.H. 2004, *ApJS*, 155, 675
- Kataoka, J., Reeves, J.N., Iwasawa, K. et al. 2007, *PASJ*, 59, 279
- Kim, C. 2001, *JApA*, 22, 283
- Kinney, A., Antonucci, R.R.J., Ward, M.J., Wilson, A.S., Whittle, M. 1991, *ApJ*, 377, 100
- Komossa, S. & Fink, H. 1997a, *A&A*, 322, 719
- Komossa, S. & Fink, H. 1997b, *A&A*, 327, 483
- Komossa, S. 2002, *Workshop on X-ray Spectroscopy of AGN with Chandra and XMM-Newton*, held at MPE Garching, December 3-6, 2001, *MPE Report* 279, p. 113
- Kortright, J.B., & Kim, S.-K. 2000, *Phys. Rev. B*, 62, 12216
- Kraemer, S. et al. 2000, *ApJ*, 535, 53
- Krongold, Y., Nicastro, F., Elvis, M., Brickhouse, N., Binette, L., Mathur, S. & Jiménez-Bailón, E. 2007, *ApJ*, 659, 1022
- Kukula, M.J. et al. 1995, *MNRAS*, 276, 1262
- Laor, A. 1991, *ApJ*, 376, 90
- Lamer, G., Uttley, P. & McHardy, I.M. 2003, *MNRAS*, 342, L41
- Lee, J.C., Ogle, P.M., Canizares, C., Marshall, H., Schulz, N.S., Morales, R., Fabian, A.C. & Iwasawa, K. 2001, *ApJ*, 544, L13
- Liu, B.F., Taam, R., Meyer-Hofmeister, E. & Meyer, F. 2007, *ApJ*, 671, 695
- Lodders, K. 2003, *ApJ*, 591, 1220
- Lyubarskii, Y.E. 1997, *MNRAS*, 292, 679
- Magdziarz, P. & Zdziarski, A. 1995, *MNRAS*, 273, 837
- Magdziarz, P., Blaes, O., Zdziarski, A.A., Johnson, W.N. & Smith, D.A. 1998, *MNRAS*, 301, 179
- Markowitz, A., Edelson, R. & Vaughan, S. 2003, *ApJ*, 598, 935
- Markowitz, A., Reeves, J.N. & Braito, V. 2006, *ApJ*, 646, 783
- Markowitz, A., Takahashi, T., Watanabe, S. et al. 2007, *ApJ*, 665, 209
- Markowitz, A., Reeves, J.N., Miniutti, G., Serlemitsos, P., Kunieda, H., Yaqoob, T., Fabian, A.C., Fukazawa, Y., et al. 2008, *PASJ*, 60S, 277
- Marscher, A. et al. 2008, *Nature*, 452, 966
- Morrison, R. & McCammon, D. 1983, *ApJ*, 270, 119
- Mould, J.R., Huchra, J.P., Freedman, W. et al. 2000, *ApJ*, 529, 786
- Mundell, C., Pedlar, A., Axon, D.J., Meaburn, J. & Unger, S.W. 1995b, *MNRAS*, 277, 641
- Mundell, C., Holloway, A., Pedlar, A., Meaburn, J., Kukula, M.J. & Axon, D.J., 1995a, *MNRAS*, 275, 67
- Murphy, E.M., Lockman, F.J., Laor, A. & Elvis, M. 1996, *ApJS*, 105, 369
- Narayan, R., Igumenshchev, I.V. & Abramowicz, M.A. 2000, *ApJ*, 539, 798
- Narayan, R. & Yi, I. 1994, *ApJ*, 428, L13
- Narayan, R. & Yi, I. 1995, *ApJ*, 452, 710
- Netzer, H. 1990, in *Active Galactic Nuclei*, ed. R.D. Blandford, H. Netzer, & L. Woltjer (Berlin: Springer), 107
- Netzer, H. 1996, *ApJ*, 473, 781
- Netzer, H., Maoz, D., Laor, A. et al. 1990, *ApJ*, 353, 108
- Netzer, H., Turner, T.J. & George, I.M. 1994, *ApJ*, 435, 106
- Peterson, B. et al. 1998, *PASP*, 110, 660
- Peterson, B.M., Ferrarese, L., Gilbert, K.M., Kaspi, S., Malkan, M., Maoz, D., Merritt, D., Netzer, H. et al. 2004, *ApJ*, 613, 682
- Pollack, A.M.T. et al. 2007, "Status of the RGS Calibration," *XMM-SOC-CAL-TN-0030*
- Porquet, D. & Dubau, J. 2000, *A&AS*, 143, 495
- Porquet, D., Reeves, J.N., Uttley, P., Turner, T.J. 2004, *A&A*, 427, 101
- Porter, R. & Ferland, G. 2007, *ApJ*, 664, 586
- Protassov, R., van Dyk, D.A., Connors, A., Kashyap, V.L. & Siemiginowska, A. 2002, *ApJ*, 571, 545
- Ptak, A., Yaqoob, T., Serlemitsos, P., Mushotzky, R. & Otani, C. 1994, *ApJ*, 436, L31
- Puccetti, S., Fiore, F., Risaliti, G., Capalbi, M., Elvis, M. & Nicastro, F. 2007, *MNRAS*, 377, 607
- Reynolds, C.S. 1997, *MNRAS*, 286, 513
- Risaliti, G., Elvis, M., Fabbiano, G., Baldi, M., Zezas, A. 2005, *ApJ*, 623, L93
- Risaliti, G., Elvis, M., Nicastro, F. 2002, *ApJ*, 571, 234
- Ross, R.R., Fabian, A.C. 2005, *MNRAS*, 358, 211
- Rothschild, R. et al. 1998, *ApJ*, 496, 538
- Rubin, V.C. & Ford, W.K. 1968, *ApJ*, 154, 431
- Schmitt, H. & Kinney, A. 1996, *ApJ*, 463, 498
- Schulz, N.S., Cui, W., Canizares, C.R., Marshall, H.L., Lee, J.C., Miller, J.M. & Lewin, W.H.G. 2002, *ApJ*, 565, 1141
- Shakura, N.I. & Sunyaev, R.A. 1973, *A&A*, 24, 337
- Shull, J.M. & van Steenburg, M.E. 1985, *ApJ*, 294, 599
- Smith, R. & Vaughan, S. 2007, *MNRAS*, 375, 1479
- Snow, T.P. & Witt, A.N. 1996, *ApJ*, 468, L65
- Strüder, L. et al. 2001, *A&A*, 365, L18
- Suganuma, M., Yoshii, Y., Kobayashi, Y., Minezaki, T., Enya, K., Tomita, H., Aoki, T., Koshida, K. & Peterson, B.A. 2006, *ApJ*, 639, 46
- Sunyaev, R. & Titarchuk, L. 1980, *A&A*, 86, 121
- Swank, J. 1998, in *Nuclear Phys. B (Proc. Suppl.): The Active X-ray Sky: Results From BeppoSAX and Rossi-XTE*, Rome, Italy, 1997 October 21-24, eds. L. Scarsi, H. Bradt, P. Giommi & F. Fiore, *Nucl. Phys. B Suppl. Proc. (The Netherlands: Elsevier Science B.V.)*, 69, 12
- Tanaka, Y. et al. 1995, *Nature*, 375, 659
- Titarchuk, L., 1994, *ApJ*, 434, 313
- Tombesi, F., de Marco, B., Iwasawa, K., Cappi, M., Dadina, M., Ponti, G., Miniutti, G. & Palumbo, G.G.C., 2007, *A&A*, 467, 1057
- Turner, M.J.L. et al. 2001, *A&A*, 365, L27
- Turner, T.J., Reeves, J.N., Kraemer, S.B. & Miller, L. 2008, *A&A*, 483, 161
- Urry, C.M. & Padovani, P. 1995, *PASP*, 107, 803
- Uttley, P. & McHardy, I.M. 2005, *MNRAS*, 363, 586
- Vaughan, S., Boller, Th., Fabian, A.C., Ballantyne, D.R., Brandt, W.N. & Trümper, J. 2002, *MNRAS*, 337, 247
- Vaughan, S., Edelson, R., Warwick, R. & Uttley, P. 2003, *MNRAS*, 345, 1271
- Vaughan, S. & Fabian, A.C. 2004, *MNRAS*, 348, 1415
- Vaughan, S. & Uttley, P. 2008, *MNRAS*, submitted
- Veigle, W.M. 1973, *Atomic Data Tables*, 5, 51
- Wandel, A., Peterson, B.M. & Malkan, M.A. 1999, *ApJ*, 526, 579
- Welsh, W. 1999, *PASP*, 111, 1347
- White, R. & Peterson, B.M. 1994, *PASP*, 106, 879
- Winge, C., Peterson, B.M., Horne, K., Pogge, R.W., Pastoriza, M.G. & Storchi-Bergmann, T. 1995, *ApJ*, 445, 680
- Woo, J.-H. & Urry, C.M. 2002, *ApJ*, 579, 530
- Wozniak, P.R., Zdziarski, A.A., Smith, D., Madejski, G. & Johnson, W.N. 1998, *MNRAS*, 299, 449
- Wu, Q. & Gu, M. 2008, *ApJ*, 682, 212

TABLE 1
FE K BANDPASS COMPONENTS IN THE TIME-AVERAGED EPIC PN SPECTRUM

Component	Parameter	Value
Fe K α emission line	χ^2/dof	983.2/990
	Energy (keV)	6.403 ± 0.009
	Width σ (eV)	65 ± 14
	Intensity (ph cm $^{-2}$ s $^{-1}$)	$3.5 \pm 0.4 \times 10^{-5}$
Ni K α emission line	EW (eV)	91 ± 10
	Energy (keV)	$7.41^{+0.08}_{-0.07}$
	Intensity (ph cm $^{-2}$ s $^{-1}$)	$4^{+4}_{-3} \times 10^{-6}$
6.04 keV emission line	EW (eV)	13^{+13}_{-10}
	Energy (keV)	$6.04^{+0.20}_{-0.06}$
	Width σ (eV)	< 200
	Intensity (ph cm $^{-2}$ s $^{-1}$)	$9.1 \pm 2.5 \times 10^{-6}$
Fe K Edge	EW (eV)	22 ± 6
	Energy (keV)	7.11 (fixed)
	Optical Depth τ	0.05 ± 0.03

Note. — Parameters for the best-fitting “GA” model (wherein the emission near 6.0 keV is modeled with a narrow Gaussian component), fit to >4 keV data. The model includes a Fe K β line, with energy fixed at 7.056 keV (rest frame), width σ tied to that of the K α line, and intensity equal to 0.13 times that of the K α line. The width σ for the Ni K α line was also tied to that for the Fe K α line. Equivalent widths EW were determined relative to a locally-fit continuum.

TABLE 2
MODEL FITS TO THE 0.2–10 KEV TIME-AVERAGED EPIC PN SPECTRUM

Component	Parameter	SXPL Model	BB Model	COMPST Model
	χ^2/dof	1866.9/1724	1870.4/1724	1863.4/1723
Local cold absorption	$N_{H,local}$ (cm $^{-2}$)	$8.7^{+0.6}_{-0.5} \times 10^{20}$	$5.1^{+1.2}_{-0.2} \times 10^{20}$	$7.7^{+0.7}_{-0.3} \times 10^{20}$
Hard X-ray power-law	Γ_{HX}	1.57 ± 0.02	$1.61^{+0.01}_{-0.02}$	$1.65^{+0.02}_{-0.03}$
	Norm. (1 keV)	$6.7^{+0.3}_{-0.2} \times 10^{-3}$	$7.4 \pm 0.1 \times 10^{-3}$	$8.1^{+0.2}_{-0.5} \times 10^{-3}$
Hard X-ray Absorption	$N_{H,HX}$ (cm $^{-2}$)	$2.9^{+0.3}_{-0.8} \times 10^{21}$	$< 6.1 \times 10^{20}$	$4.2^{+0.3}_{-1.1} \times 10^{21}$
Low-ioniz. X-ray Warm Abs.	$N_{H,lo}$ (cm $^{-2}$)	$1.0^{+0.3}_{-0.1} \times 10^{21}$	$7.9^{+2.7}_{-0.7} \times 10^{20}$	$9.3^{+2.1}_{-1.9} \times 10^{20}$
	$\log \xi_{lo}$ (erg cm s $^{-1}$)	$1.45^{+0.16}_{-0.07}$	1.38 ± 0.19	$1.43^{+0.20}_{-0.43}$
High-ioniz. X-ray Warm Abs.	$N_{H,hi}$ (cm $^{-2}$)	$1.8^{+1.2}_{-0.6} \times 10^{21}$	$1.8^{+1.3}_{-0.4} \times 10^{21}$	$1.5^{+1.3}_{-0.6} \times 10^{21}$
	$\log \xi_{hi}$ (erg cm s $^{-1}$)	$2.93^{+0.15}_{-0.09}$	$2.91^{+0.15}_{-0.07}$	$2.89^{+0.14}_{-0.20}$
Soft X-ray power-law	Γ_{SX}	$3.35^{+0.27}_{-0.10}$		
	Norm. (1 keV)	$4.0^{+0.2}_{-0.7} \times 10^{-3}$		
Blackbody	Temperature $k_B T$ (eV)		83^{+1}_{-4}	
	Norm.		$1.72^{+0.37}_{-0.11} \times 10^{-4}$	
Comptonized component	Temperature $k_B T$ (keV)			$0.35^{+0.02}_{-0.03}$
	Optical Depth τ			24^{+2}_{-4}
	Norm.			$4.41^{+0.22}_{-0.33} \times 10^{-3}$
O VII emission line	Energy (keV)	0.58 ± 0.01	$0.58^{+0.02}_{-0.01}$	0.58 ± 0.01
	Intensity (ph cm $^{-2}$ s $^{-1}$)	$2.4^{+0.5}_{-0.4} \times 10^{-4}$	$1.2^{+0.6}_{-0.5} \times 10^{-4}$	$2.1 \pm 0.4 \times 10^{-4}$

Note. — SXPL, BB and COMPST refer to the models wherein the soft excess is modeled with a steep power-law component, a blackbody component, and a Comptonized component (COMPST), respectively. The units of normalization of the power-law components are ph keV $^{-1}$ cm $^{-2}$ s $^{-1}$ at 1 keV. The blackbody normalization is $L_{39} D_{10}^{-2}$, where L_{39} is the source luminosity in units of 10^{39} erg s $^{-1}$ and D_{10} is the distance to the source in units of 10 kpc. See the XSPEC user manual for units of the COMPST component normalization. The reader is reminded that the BB and COMPST models are not generally accepted as physically plausible descriptions of soft excesses in Seyferts. The uncertainties listed on the intensity of the O VII emission line are statistical only and do not include likely systematic uncertainties due to blending with narrow absorption lines. The width σ of the O VII emission line was kept fixed at 0.5 eV.

TABLE 3
EMISSION LINES FIT TO THE RGS SPECTRUM

Line Identification	Energy (eV)	Intensity (ph cm ⁻² s ⁻¹)	$\Delta\chi^2$	F -test Probability
N VI (<i>r</i>)	431 \pm 1	9.9 ^{+6.7} _{-5.0} $\times 10^{-5}$	-12.0	0.042
N VII	499 ⁺¹ ₋₂	8.2 ^{+6.0} _{-5.2} $\times 10^{-5}$	-10.4	0.064
O VII (<i>f</i>)	561 ⁺¹ ₋₂	1.33 ^{+0.13} _{-0.75} $\times 10^{-4}$	-25.2	1.4 $\times 10^{-3}$
O VII (<i>i</i>)	567 \pm 1	9.5 ^{+3.2} _{-3.5} $\times 10^{-5}$	-18.5	7.8 $\times 10^{-3}$
O VII (<i>r</i>)	572 ⁺¹ ₋₂	4.9 ^{+12.3} _{-2.9} $\times 10^{-5}$	-7.9	0.12

Note. — Best-fit line emission parameters using Gaussian components. All line widths σ were kept fixed at 0.5 eV. The uncertainties listed on the intensities (Col. [3]) are statistical only and do not include likely systematic uncertainties due to blending with narrow absorption lines. The F -test probability values P (Col. [5]) denote the changes that the null hypothesis (line not included in model) is valid; the line detection significance is $1 - P$.

TABLE 4
BEST-FIT MODEL PARAMETERS FOR THE RGS SPECTRUM

Component	Parameter	Value
	χ^2/dof	785.7/417
Local cold absorption	$N_{\text{H,local}}$ (cm ⁻²)	10.5 ^{+1.2} _{-1.9} $\times 10^{20}$
Soft X-ray power-law	Γ_{SX}	3.00 \pm 0.25
	Norm. (1 keV)	6.2 ^{+0.3} _{-0.7} $\times 10^{-3}$
Low-ioniz. X-ray Warm Abs.	$N_{\text{H,lo}}$ (cm ⁻²)	1.1 ^{+0.1} _{-0.2} $\times 10^{21}$
	$\log\xi_{\text{lo}}$ (erg cm s ⁻¹)	1.21 ^{+0.18} _{-0.08}
	z_{lo} (absolute)	+0.00246 ^{+0.00144} _{-0.00064}
	z_{lo} (rel. to systemic)	-0.00140 ^{+0.00144} _{-0.00064}
High-ioniz. X-ray Warm Abs.	$N_{\text{H,hi}}$ (cm ⁻²)	2.4 ^{+2.0} _{-1.2} $\times 10^{21}$
	$\log\xi_{\text{hi}}$ (erg cm s ⁻¹)	2.90 ^{+0.21} _{-0.26}
	z_{hi} (absolute)	-0.00302 ^{+0.00057} _{-0.00080}
	z_{hi} (rel. to systemic)	-0.00688 ^{+0.00057} _{-0.00080}

Note. — Results are shown for the best-fit soft X-ray power-law model, including five emission lines due to He-like O and H- and He-like N; see Table 3 for emission line parameters. The units of normalization of the power-law components are ph keV⁻¹ cm⁻² s⁻¹ at 1 keV. See text for details regarding uncertainty range in z . The model also included a hard X-ray power-law component absorbed by a column $N_{\text{H,HX}} \sim 8 \times 10^{21}$ cm⁻² and emerging only above ~ 1.5 keV.

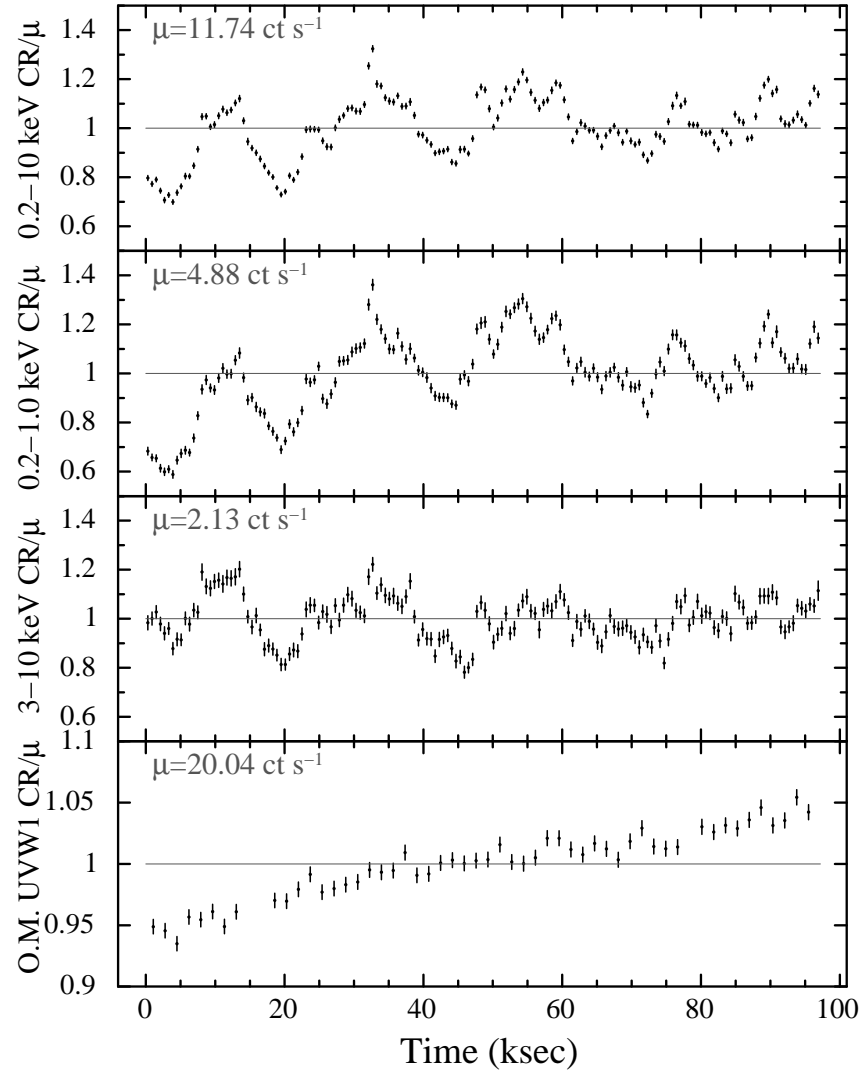


FIG. 1.— The top three panels show the EPIC-pn count rate light curves for the 0.2–10, 0.2–1, and 3–10 keV bandpasses, binned to 600 s. The bottom panel shows the OM UVW1 light curve, binned to 1400 s.

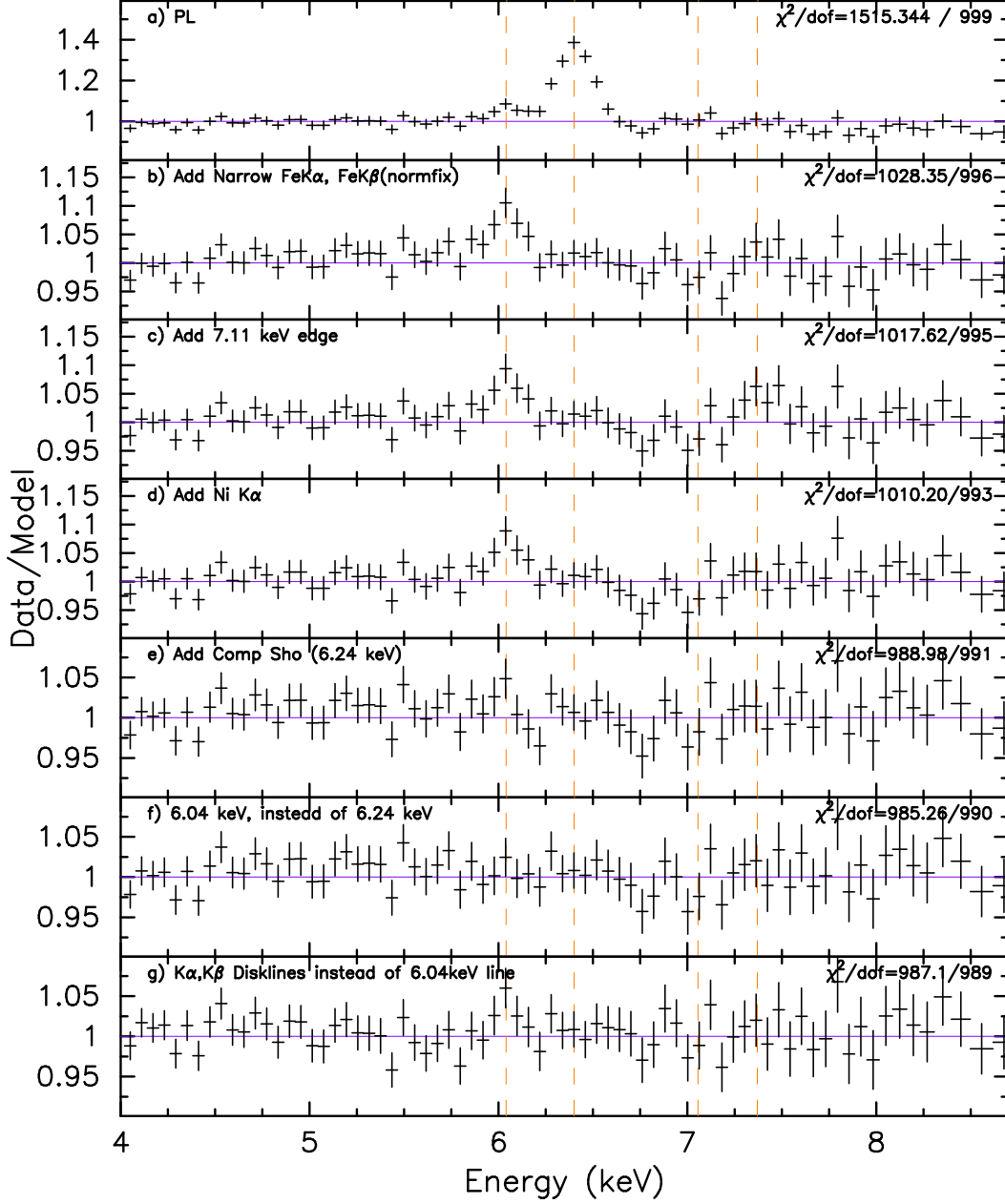


FIG. 2.— Data/model residuals to spectral fits to the Fe K bandpass of the EPIC-pn spectrum. Data are rebinned by a factor of 12. Vertical dashed lines denote energies of 6.04, 6.40, 7.06, and 7.37 keV. Panel *a*) shows residuals to a simple power-law model. In panel *b*), the Fe K α and Fe K β emission lines have been modeled. The 7.11 keV edge and Ni K α line have been modeled in panels *c*) and *d*), respectively. In panel *e*), a Gaussian with an energy centroid of 6.24 keV has been added. However, as shown in panel *f*), the best-fit “GA” model, with a Gaussian with an energy centroid at 6.04 keV, does a superior job in modeling the remaining ~ 6 keV residuals. The small dip near 6.8 keV is not significant and is likely an artifact of fitting. In panel *g*), the best-fit “DL” model, the 6.04 keV line has been removed and replaced with relativistically broadened Fe K α and Fe K β diskline profiles; the narrow Gaussian at 6.04 keV (panel *f*)) seems to model the residuals better.

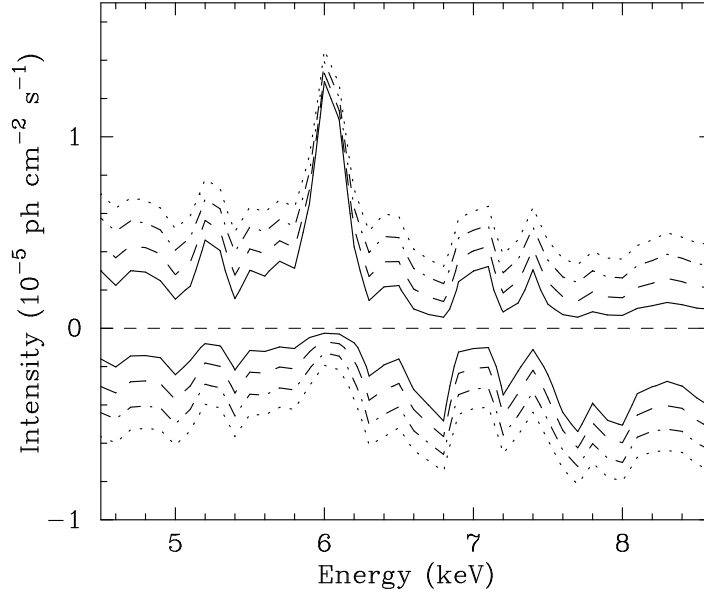


FIG. 3.— Contour plots showing the results of applying a “sliding Gaussian” (with width σ fixed at 10 eV) to a model to the EPIC-pn data consisting of a power-law plus a narrow Gaussian at 6.40 keV to model Fe K α emission. 1-, 2-, 3- and 4- σ confidence levels for two interesting parameters are denoted by solid, dashed, dot-dashed, and dotted lines, respectively. Residuals near 6.0 keV are clear; additional residuals at 7.0 and 7.4 keV (above the Fe K edge at 7.11 keV) are investigated further in §3.

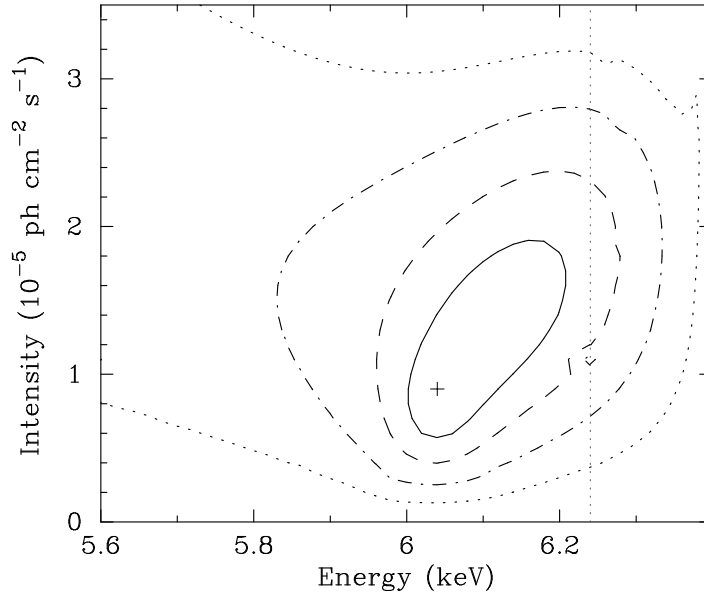


FIG. 4.— Contour plot of intensity versus line centroid energy for the Gaussian used to model the narrow 6.0 keV emission feature in the pn spectrum. The width σ was left as a free parameter. 1-, 2-, 3- and 4- σ confidence levels for two interesting parameters are denoted by solid, dashed, dot-dashed, and dotted lines, respectively.

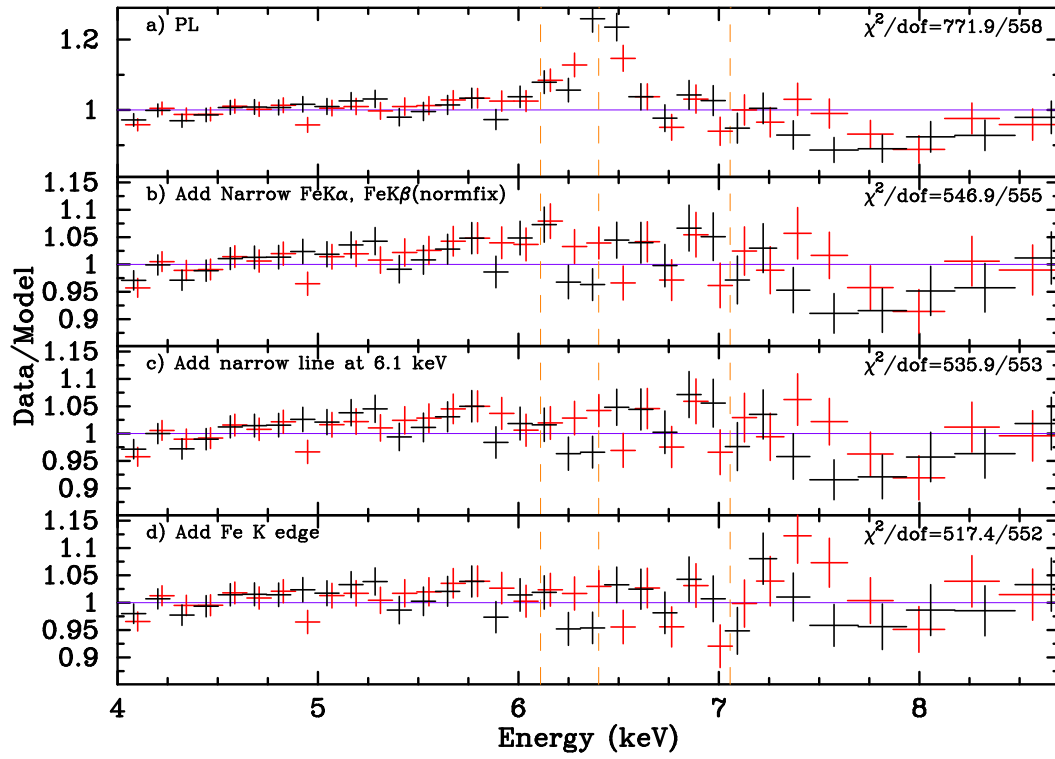


FIG. 5.— Data/model residuals to various model fits to the MOS 1+2 spectrum. Data are rebinned by a factor of 8. Panel *a*) shows residuals to a simple power-law model. In panel *b*), the Fe K α and Fe K β emission lines have been modeled. In panels *c*) and *d*), respectively, the 6.11 keV emission line and the Fe K edge have been added.

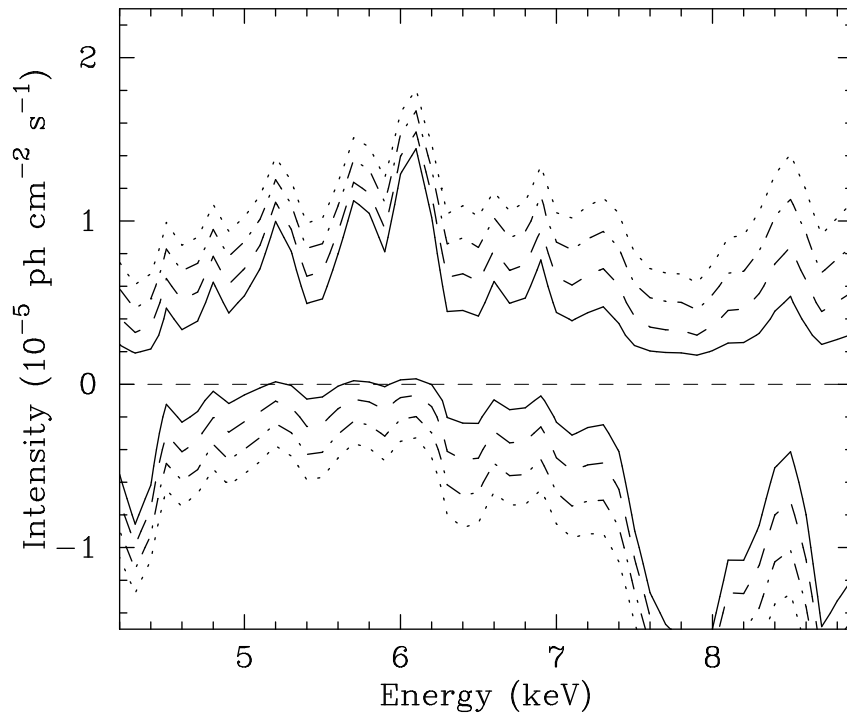


FIG. 6.— Same as Figure 3, but for the MOS 1+2 spectral fitting.

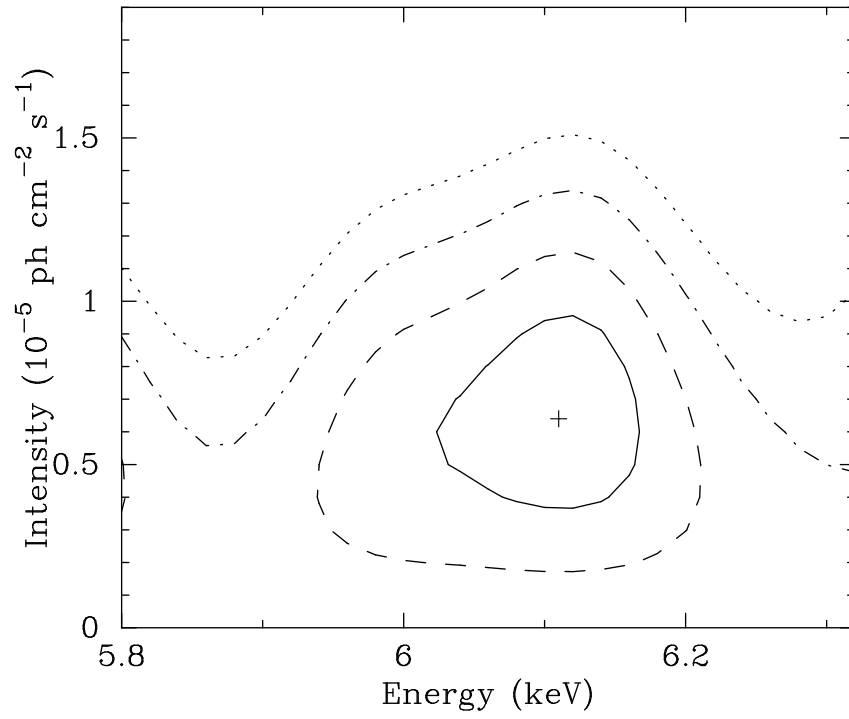


FIG. 7.— Contour plot of intensity versus line centroid energy for the Gaussian used to model the narrow 6.1 keV emission feature in the MOS 1+2 spectrum. The width σ was left as a free parameter. 1-, 2-, 3- and 4- σ confidence levels for two interesting parameters are denoted by solid, dashed, dot-dashed, and dotted lines, respectively.

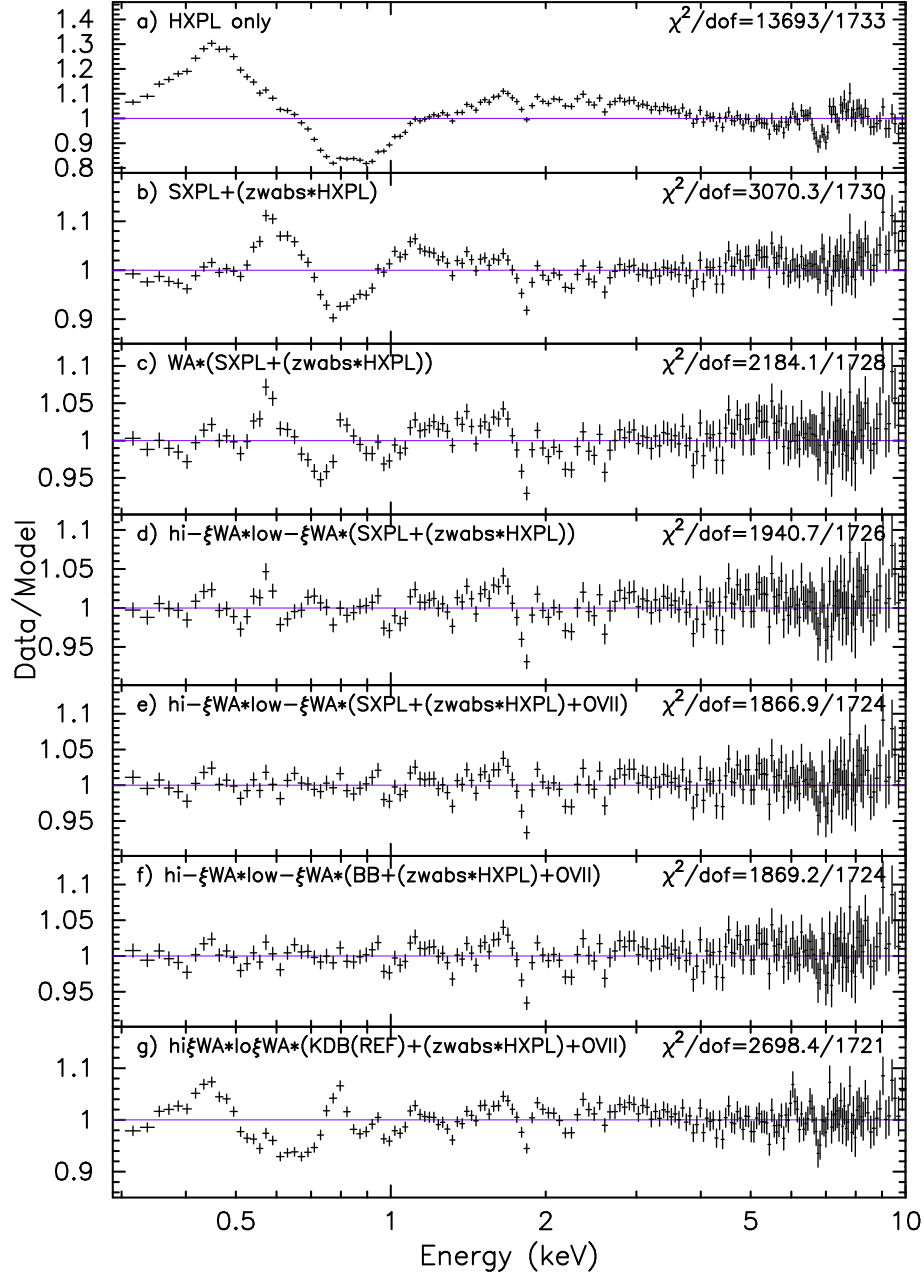


FIG. 8.— Data/model residuals to spectral fits to the 0.2–10 keV EPIC-pn spectrum. All models include narrow Gaussian components to model the Fe $K\alpha$, Fe $K\beta$, Ni $K\alpha$ and 6.04 keV emission lines, an Fe K edge at 7.11 keV, and a column of neutral gas to model Galactic absorption. Panel *a*) shows the results when a simple hard X-ray power-law component (HXPL) is used. In Panel *b*), a neutral absorbing column has been added to the HXPL, and a steep, soft X-ray power-law component (SXPL) has been added. In panels *c*) and *d*), the low- and hi-ionization warm absorbers, respectively, have been included. In panel *e*), a narrow Gaussian to model O VII emission has been included; this is the best-fitting “SXPL” model. In panel *f*), the soft power-law has been replaced with a blackbody component; this is the best-fitting “BB” model. Panel *g*) shows the results from modeling the soft excess as blurred reflection from an ionized disk. (The small dip near 6.8 keV is not significant and is likely an artifact of fitting.)

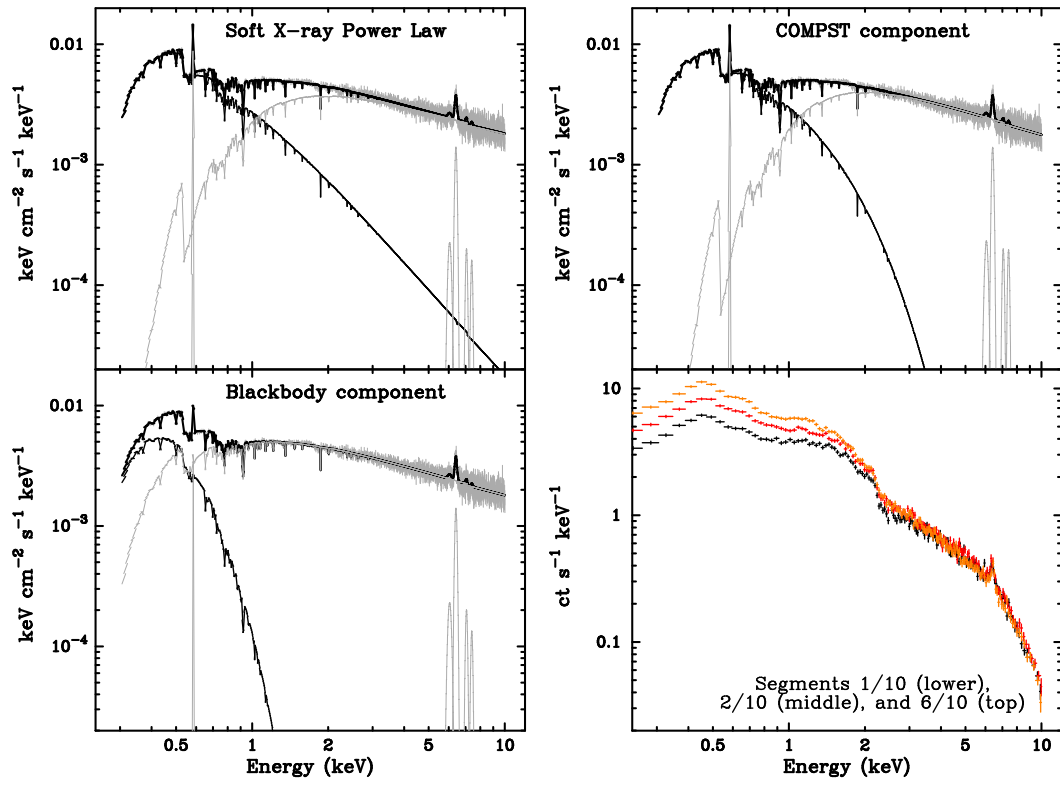


FIG. 9.— Unfolded spectra for the best-fitting SXPL, BB and COMPST models. Panel *d*) shows the spectra for three selected time-resolved segments, further illustrating the increase in soft X-ray flux between segments 1, 2 and 6.

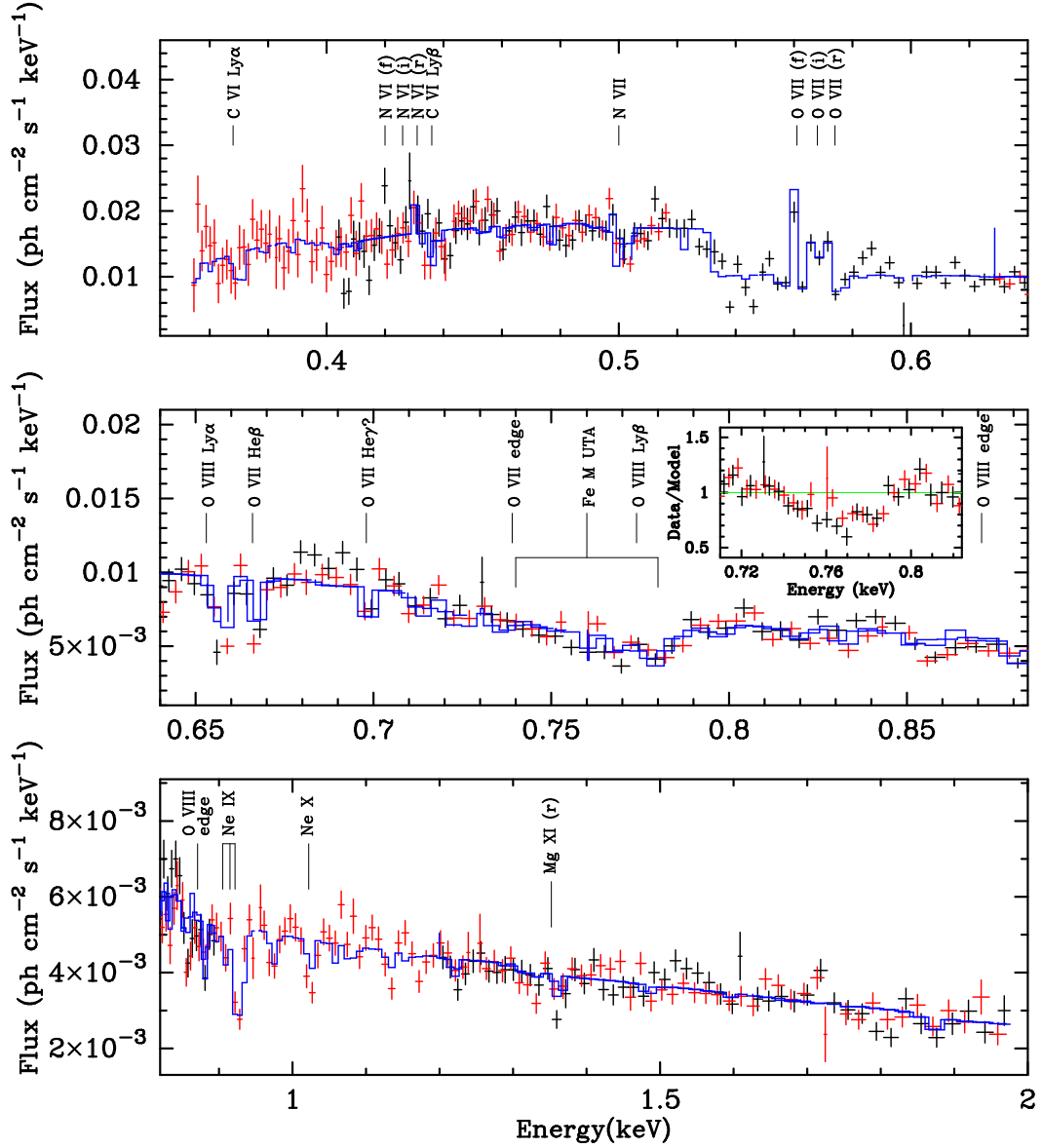


FIG. 10.— The RGS spectrum for NGC 3227. The solid line shows the best-fitting unfolded model, described in §5. Data have been rebinned by a factor of 2, and are plotted in the rest frame. Black and red data points denote RGS 1 and 2, respectively. The vertical lines, which indicate identified lines and edges, denote rest-frame (systemic) energies. The residuals near 687 and 850 eV are instrumental artifacts.

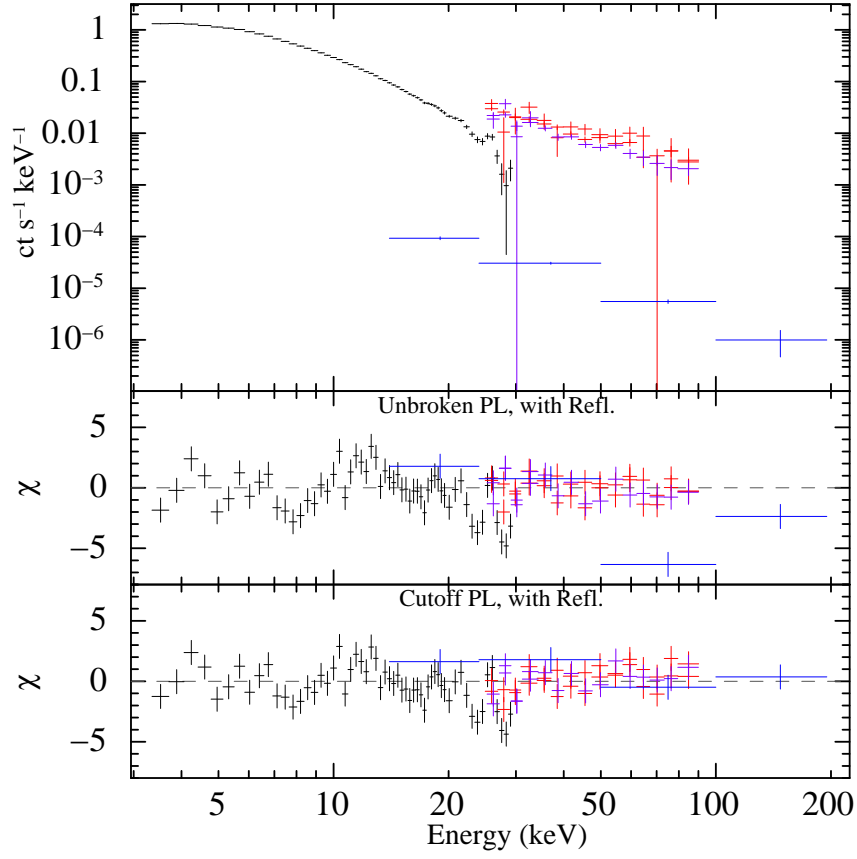


FIG. 11.— The upper panel shows the *RXTE*-PCA (black), *RXTE*-HEXTE cluster A (red) and B (purple), and *Swift*-BAT data (blue). The middle and lower panels show χ residuals to the best-fit models with and without a high-energy cutoff in the power-law component, respectively. In each case, the model contains a Compton reflection component and Fe $K\alpha$ emission.

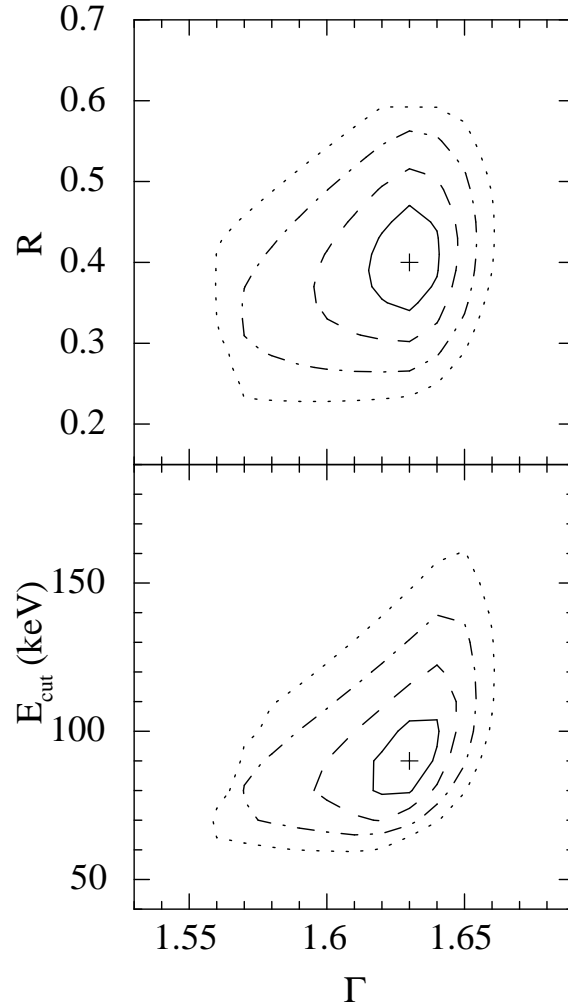


FIG. 12.— Contour plots showing the strength of the Compton reflection component, R (measured via a PEXRAV component; top panel) and cutoff energy (bottom) versus hard X-ray photon index from spectral fits to *RXTE* PCA and HEXTE and *Swift*-BAT data. 1-, 2-, 3- and 4- σ confidence levels for two interesting parameters are denoted by solid, dashed, dot-dashed, and dotted lines, respectively.

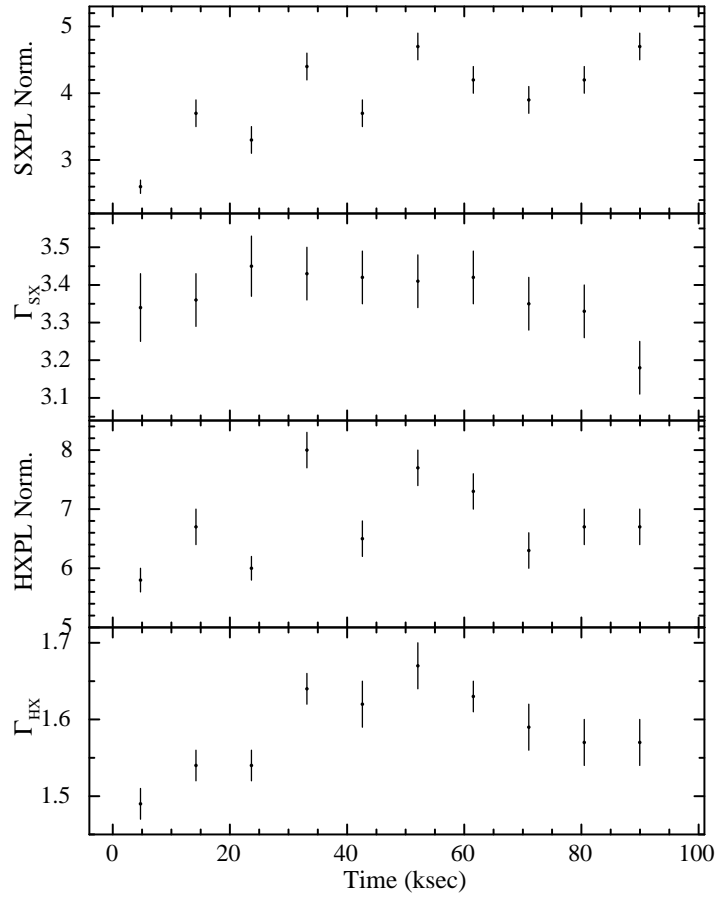


FIG. 13.— The results of fitting the SXPL model to the ten time-resolved spectral segments. From top to bottom: Normalization of the soft X-ray power-law component, Γ_{SX} , normalization of the hard X-ray power-law component, and Γ_{HX} .

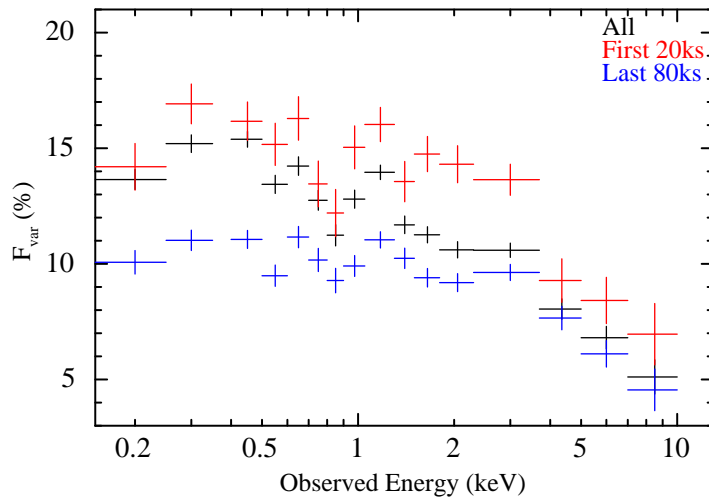


FIG. 14.— F_{var} spectra derived from EPIC-pn data for the entire duration (black), the first 20 ks (red) and the final 80 ks (blue).

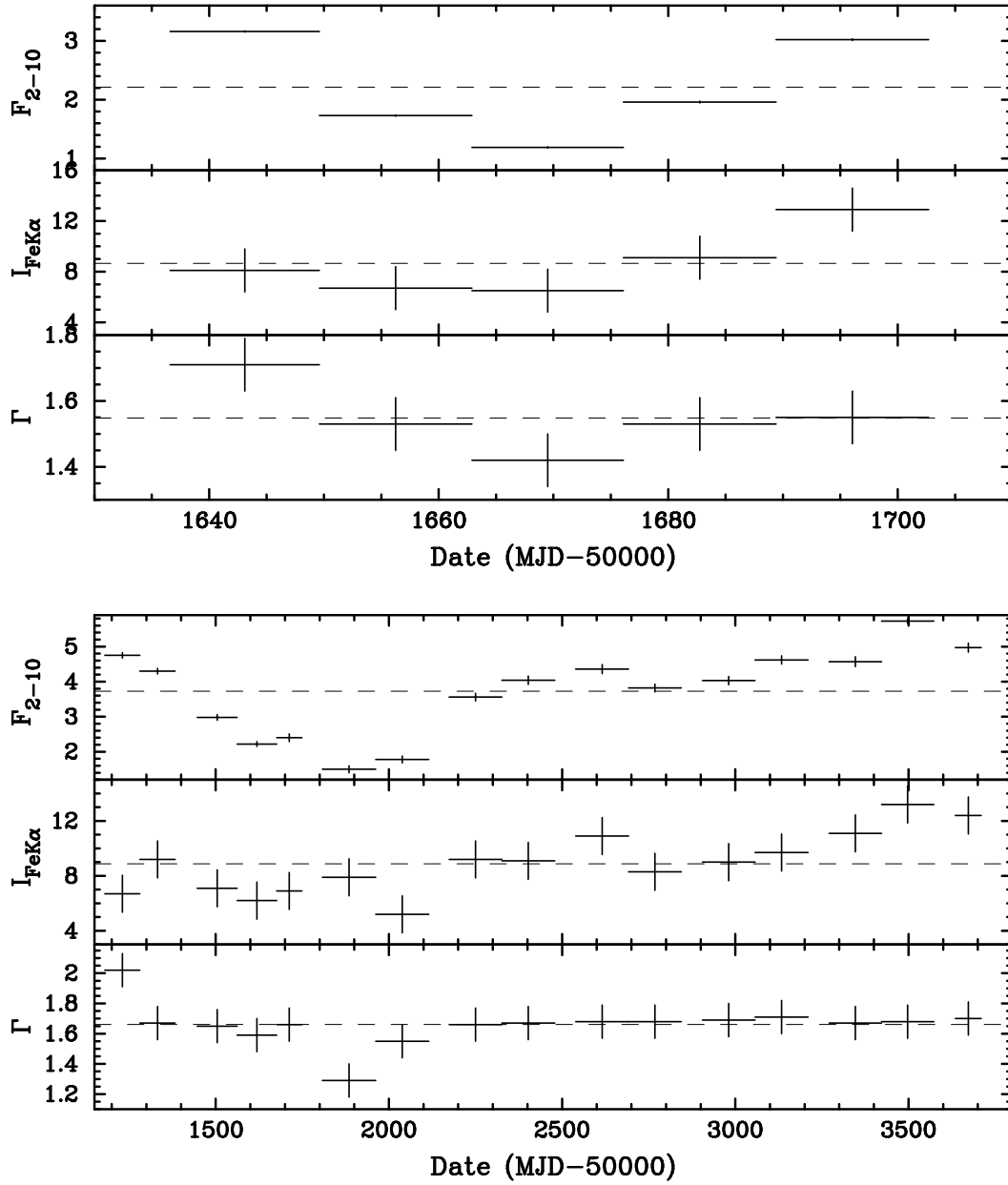


FIG. 15.— The results of time-resolved spectral fits to the medium-term (top) and long-term (bottom) *RXTE* data, showing 2–10 keV continuum flux in units of 10^{-11} erg cm $^{-2}$ s $^{-1}$, Fe K line intensity $I_{\text{FeK}\alpha}$ in units of 10^{-5} ph cm $^{-2}$ s $^{-1}$, and Γ_{HX} .

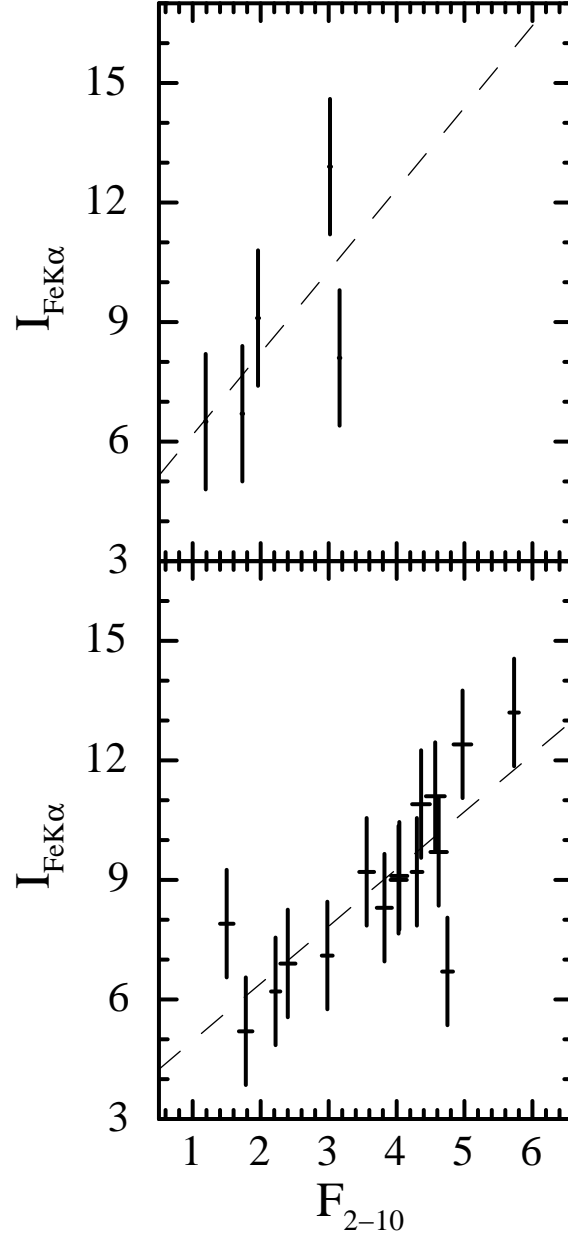


FIG. 16.— Zero-lag correlation diagrams in which Fe line intensity $I_{\text{FeK}\alpha}$, in units of 10^{-5} ph cm $^{-2}$ s $^{-1}$, is plotted against 2–10 keV continuum flux in units of 10^{-11} erg cm $^{-2}$ s $^{-1}$. Dashed lines indicate the best-fitting linear model.

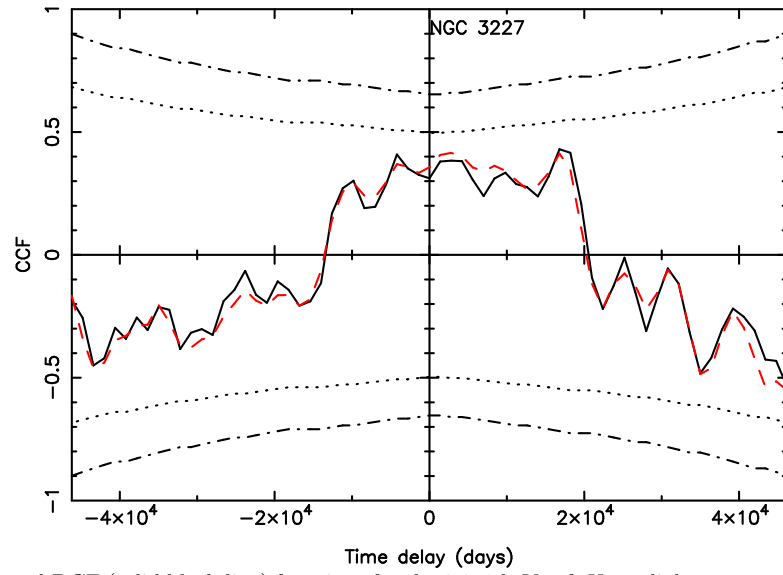


FIG. 17.— ICF (red dashed line) and DCF (solid black line) functions for the 0.2–1 keV soft X-ray light curve versus the OM UV continuum light curve (positive lag indicates soft X-ray leading the UV.)